



Small and Large Dust Cavities in Disks around Mid-M Stars in Taurus

Yangfan Shi (施杨帆)^{1,2,3} , Feng Long (龙凤)^{4,16} , Gregory J. Herczeg (沈雷歌)^{1,2} , Daniel Harsono⁵ , Yao Liu⁶ , Paola Pinilla⁷ , Enrico Ragusa^{8,9} , Doug Johnstone^{10,11} , Xue-Ning Bai¹² , Ilaria Pascucci⁴ , Carlo F. Manara³ , Gijs D. Mulders^{13,14} , and Lucas A. Cieza¹⁵

¹ Kavli Institute for Astronomy and Astrophysics, Peking University, Beijing 100871, People's Republic of China

² Department of Astronomy, Peking University, Beijing 100871, People's Republic of China

³ European Southern Observatory, Karl-Schwarzschild-Str. 2, D-85748 Garching bei München, Germany

⁴ Lunar and Planetary Laboratory, University of Arizona, Tucson, AZ 85721, USA

⁵ Institute of Astronomy, Department of Physics, National Tsing Hua University, Hsinchu, Taiwan

⁶ Purple Mountain Observatory & Key Laboratory for Radio Astronomy, Chinese Academy of Sciences, Nanjing 210023, People's Republic of China

⁷ Mullard Space Science Laboratory, University College London, Holmbury St Mary, Dorking, Surrey RH5 6NT, UK

⁸ Dipartimento di Matematica, Università degli Studi di Milano, Via Saldini 50, 20133, Milano, Italy

⁹ Univ Lyon, Univ Lyon1, Ens de Lyon, CNRS, Centre de Recherche Astrophysique de Lyon UMR5574, F-69230 Saint-Genis-Laval, France

¹⁰ NRC Herzberg Astronomy and Astrophysics, 5071 West Saanich Rd., Victoria, BC V9E 2E7, Canada

¹¹ Department of Physics and Astronomy, University of Victoria, Victoria, BC V8P 5C2, Canada

¹² Institute for Advanced Study and Department of Astronomy, Tsinghua University, 100084, Beijing, People's Republic of China

¹³ Facultad de Ingeniería y Ciencias, Universidad Adolfo Ibáñez, Av. Diagonal las Torres 2640, Peñalolén, Santiago, Chile

¹⁴ Millennium Institute for Astrophysics, Chile

¹⁵ Instituto de Estudios Astrofísicos, Facultad de Ingeniería y Ciencias, Universidad Diego Portales, Av. Ejército 441, Santiago, Chile

Received 2023 September 30; revised 2024 February 27; accepted 2024 February 27; published 2024 April 25

Abstract

High angular resolution imaging by Atacama Large Millimeter/submillimeter Array (ALMA) has revealed the near universality and diversity of substructures in protoplanetary disks. However, disks around M-type pre-main-sequence stars are still poorly sampled, despite the prevalence of M dwarfs in the Galaxy. Here we present high-resolution (~ 50 mas, 8 au) ALMA Band 6 observations of six disks around mid-M stars in Taurus. We detect dust continuum emission in all six disks, ^{12}CO in five disks, and ^{13}CO line in two disks. The size ratios between gas and dust disks range from 1.6 to 5.1. The ratio of about 5 for 2M0436 and 2M0450 indicates efficient dust radial drift. Four disks show rings and cavities, and two disks are smooth. The cavity sizes occupy a wide range: 60 au for 2M0412, and ~ 10 au for 2M0434, 2M0436, and 2M0508. Detailed visibility modeling indicates that small cavities of 1.7 and 5.7 au may hide in the two smooth disks 2M0450 and CIDA 12. We perform radiative transfer fitting of the infrared spectral energy distributions to constrain the cavity sizes, finding that micron-sized dust grains may have smaller cavities than millimeter grains. Planet-disk interactions are the preferred explanation to produce the large 60 au cavity, while other physics could be responsible for the three ~ 10 au cavities under current observations and theories. Currently, disks around mid- to late M stars in Taurus show a higher detection frequency of cavities than earlier-type stars, although a more complete sample is needed to evaluate any dependence of substructure on stellar mass.

Unified Astronomy Thesaurus concepts: [Protoplanetary disks \(1300\)](#); [Planetary-disk interactions \(2204\)](#); [Planetary system formation \(1257\)](#)

1. Introduction

The discovery to date of over 5000 exoplanets reveals that planetary systems occupy a wide parameter space in architecture (Zhu & Dong 2021). In planetary systems around low-mass stars (e.g., lower than $0.4 M_{\odot}$), small planets occur more frequently than those around solar-mass stars (e.g., Mulders et al. 2015; Hardegree-Ullman et al. 2019), while giant planets around those low-mass stars are rare (but have a nonzero occurrence rate; e.g., Bryant et al. 2023).

The existence of a few giant planets around mid- to late (later than M3) M stars has challenged the core accretion planet formation theory (e.g., Morales et al. 2019; Stefánsson et al. 2023). Planet population synthesis simulations often fail to

form any giant planet around these very low mass stars, in both the planetesimal accretion case (e.g., Miguel et al. 2020) and the pebble accretion case (e.g., Liu et al. 2019; Burn et al. 2021; Mulders et al. 2021; Schlecker et al. 2022). Special circumstances, such as a reduction in the type I migration velocities by a factor of 10, are needed to form planetary cores more massive than $10 M_{\oplus}$ (Burn et al. 2021; Schlecker et al. 2022), which then leads to the runaway gas accretion that enables giant planet formation (Pollack et al. 1996). Besides core accretion, direct collapse in gravitationally unstable disks may also form giant planets at early stages (e.g., Boss 1997; Mercer & Stamatellos 2020; Boss & Kanodia 2023; Longarini et al. 2023), when those class 0/I protostellar disks have higher disk mass than their later-stage counterparts (e.g., Tobin et al. 2020; Tychoniec et al. 2020). Possible evidence of gravitational instability has been found in some recent Atacama Large Millimeter/submillimeter Array (ALMA) observations, even though they targeted higher-mass stars than the mid- to late M stars focused on in this work (e.g., Pérez et al. 2016; Paneque-Carreño et al. 2021; Weber et al. 2023).

¹⁶ NASA Hubble Fellowship Program Sagan Fellow.

Table 1
Properties of Host Stars

2MASS Short Name	D (pc)	SpT	A_V (mag)	J	L_{phot} (L_{\odot})	M_* (M_{\odot})	R_* (R_{\odot})	L_{acc} (L_{\odot})	M_{acc} ($M_{\odot} \text{ yr}^{-1}$)	References
J04124068+2438157 2M0412	148.7	M4.3	0.84	11.151	0.126	0.30	1.21	0.00204	3.2E-10	L23
J04343128+1722201 2M0434	145.7	M4.3	0.30	11.205	0.115	0.30	1.16	0.00168	2.6E-10	...
J04360131+1726120 2M0436	144.5	M2.7	1.08	11.105	0.146	0.58	1.07	0.0062	4.5E-10	...
J04504003+1619460 2M0450	144.4	M4.75	0.0	11.725	0.054	0.24	0.84	L18
J05075496+2500156 CIDA 12	170.0	M3.7	0.5	11.415	0.13	0.39	1.13	0.0028	3.2E-10	HH14
J05080709+2427123 2M0508	170.7	M3.5	0.0	11.396	0.11	0.44	1.03	L18

References. L23: Long et al. (2023); L18: Luhman (2018); HH14: Herczeg & Hillenbrand (2014).

In the past decade, high angular resolution observations with ALMA have revealed that substructures are common in protoplanetary disks. These substructures are mostly seen as rings and gaps (e.g., ALMA Partnership et al. 2015; Andrews et al. 2018a; Long et al. 2018; Cieza et al. 2021); asymmetric substructures like arcs and spiral arms are also found but are relatively rare (e.g., van der Marel et al. 2013; Dong et al. 2018; Huang et al. 2018b). These substructures are expected to be induced by various disk physical processes and planet–disk interactions (see reviews by Andrews 2020; Bae et al. 2023). The prevalence of rings suggests the presence of pressure bumps that halt the inward radial drift of the dust (Pinilla et al. 2012).

Thus far these conclusions are obtained mostly from observations of solar-type stars and Herbig stars. For disks around M stars, the dust drift should be faster (Pinilla et al. 2013), so their disks may need stronger pressure bumps to trap dust particles in order to explain their millimeter emission at ages of a few megayears (e.g., van der Plas et al. 2016; Sanchis et al. 2020).

However, only little is known about substructures in disks around mid- to late M stars. Most structured disks around M dwarf stars show rings and gaps (González-Ruilova et al. 2020; Cieza et al. 2021; Kurtovic et al. 2021; Pinilla et al. 2021; van der Marel et al. 2022), where the gaps are mostly central cavities or large gaps surrounding a compact inner disk (Pinilla 2022). Only one disk around a mid-M dwarf shows a clear asymmetric ring, with properties similar to asymmetries found around T Tauri and Herbig AeBe stars (Hashimoto et al. 2021). Detailed hydrodynamical simulations toward the disk around the mid-M dwarf CIDA 1 suggest that a planet with a minimum mass of $\sim 1.4M_{\text{Jup}}$ is needed to carve out the observed cavities present in 0.9 and 2.1 mm continuum images (Curone et al. 2022), challenging the core accretion planet formation theory around very low mass stars.

Following the pilot studies above, additional deep high-resolution observations on disks around M stars (or very low mass stars) are needed to evaluate the dust morphology and test disk physical processes in extreme situations, following similar strategies applied to solar-mass stars (e.g., Andrews et al. 2018a; Cieza et al. 2019; Long et al. 2019). This paper presents observations from a program designed to obtain high-resolution observations ($\sim 0''.05$) of 16 mid-M star disks in the Taurus star-forming region. Of the proposed targets, we have obtained observations of six disks, including the double-ringed disk of 2MASS J04124068+2438157, which was presented in Long et al. (2023). Here we present all six observed disks (including 2M0412 from Long et al. 2023) to study properties of substructures in M star disks and their possible origins.

The paper is organized as follows: In Section 2, we describe our target selection, ALMA observations, data reduction, and calibration. In Section 3, we present our modeling method in the visibility plane and the modeling results, as well as CO gas measurement. Section 4 discusses the global properties of the six disks and possible origins for their detected substructures. In Section 5 we summarize our main findings.

2. ALMA Program and Observations

2.1. Sample Selection and Properties

We analyze disks observed in the ALMA project 2019.1.00566.S (PI: G. Herczeg), which aimed at studying the dependence of dust substructure properties on stellar mass by targeting 16 disks around M3–M5 stars selected from Taurus. The sample selection started from Luhman et al. (2017) with disk identification based on excess emission in Wide-field Infrared Survey Explorer (WISE) W2 and W3 bands. We excluded known binaries (e.g., Kraus et al. 2011; Daemgen et al. 2015) and sources with $A_V > 3$ mag or J -band brightness 1 mag fainter than the median to avoid edge-on disks and embedded objects. Furthermore, targets with decl. $> 26^\circ$ are excluded for visibility purposes. Like Long et al. (2019), the selection ignored the millimeter brightness of disks. Six out of the 16 proposed targets were observed with the C43-9/10 configuration and Band 6 receivers between 2021 August 27 and 2021 September 27.

For these six sources, their stellar properties (listed in Table 1) were reevaluated based on optical spectra when available. For 2M0450 and 2M0508, the spectral type and extinction are obtained from Luhman (2018), with uncertain accretion properties. We obtained flux-calibrated low-resolution optical spectra for 2M0412, 2M0434, and 2M0436 using UH88/SNIFS (3200–10000 Å; Lantz et al. 2004) and for 2M0507 (CIDA 12) using Palomar-Hale 5 m/DBSP (3200–8700 Å, with a gap from 5600 to 6250 Å; Oke & Gunn 1982). The SNIFS data reduction is described by Guo et al. (2018), while the DBSP data reduction is described by Herczeg & Hillenbrand (2014). For these four targets, the spectral type, extinction, and accretion rate are calculated from a simultaneous fit, following approaches described in Herczeg & Hillenbrand (2008, 2014) and using a plane-parallel slab model for accretion developed by Valenti et al. (1993). The properties of 2M0412 were presented in Long et al. (2023).

The spectral type for each star is converted to temperature using the relationship of Herczeg & Hillenbrand (2014). The luminosity is then calculated from the 2MASS J -band magnitude (Cutri et al. 2003) and assuming zero J -band veiling, J -band bolometric corrections from Pecaut & Mamajek (2013), and

Table 2
Summary of ALMA Observations

Source	Obs. Date	N_{ant}	Baselines (m)	On-source Time (minutes)	Mean PWV (mm)	Peak I_ν (Taper) (mJy beam $^{-1}$)	rms Noise (Taper) (mJy beam $^{-1}$)	Beam (Taper) (mas \times mas, deg)
2M0412	2021-08-27	38	92.1–10803.3	16.80	0.3	0.19 (0.26)	0.032 (0.039)	$74 \times 35, 37 (76 \times 73, 32)$
2M0434	2021-09-27	45	70.1–14361.8	15.29	1.0	0.47 (0.69)	0.039 (0.041)	$45 \times 24, -47 (43 \times 41, -41)$
2M0436	2021-09-27	45	70.1–14361.8	15.39	1.0	0.31 (0.42)	0.037 (0.039)	$44 \times 24, -46 (43 \times 42, 38)$
2M0450	2021-09-28	47	70.1–14361.8	15.05	0.7	0.23 (0.27)	0.029 (0.029)	$36 \times 26, -40 (36 \times 36, -35)$
CIDA 12	2021-09-13	37	178.3–12594.5	16.80	0.6	0.19 (0.30)	0.031 (0.036)	$72 \times 33, 4 (76 \times 73, -9)$
2M0508	2021-09-13	37	178.3–12594.5	16.87	0.6	0.38 (0.63)	0.035 (0.039)	$65 \times 25, 4 (63 \times 60, 36)$

Note. The numbers in parentheses in the last three columns are corresponding values for uv -tapered images.

J -band extinction from the A_J/A_V ratio developed by Wang & Chen (2019). All properties are calculated from distances obtained from inverting the parallax in Gaia Collaboration et al. (2023). The masses are then estimated using the Somers et al. (2020) evolutionary tracks for pre-main-sequence stars with 51% spot coverage. These tracks lead to higher masses than standard evolutionary tracks (see discussion for 2M0412 in Long et al. 2023).

2.2. ALMA Observations

For our ALMA observations, the receivers were configured into four spectral windows, with two centered at 217.0 and 234.4 GHz for dust continuum with bandwidths of 1.875 GHz and the other two centered at 220.0 and 230.5 GHz targeting ^{12}CO , ^{13}CO , and $\text{C}^{18}\text{O } J=2-1$ lines. Line channel intervals are spaced at 0.244 MHz ($\sim 0.3 \text{ km s}^{-1}$). Table 2 shows the detailed ALMA observation log.

The raw visibilities were pipeline calibrated using the specified CASA versions (6.1.1 for 2M0412, CIDA 12, and 2M0508; 6.2.1 for the rest) for each object that can be found in the QA2 report (CASA Team et al. 2022). We identified residual features of atmospheric absorption correction around channel 500 in the 234.4 GHz spectral window for all six targets and flagged corresponding channels 400–600. For dust continuum imaging, we flagged the channels within 25 km s^{-1} of the rest frame of CO lines and then averaged the data set with a channel width of 125 MHz, which is the recommended maximum bandwidth to avoid bandwidth smearing for ALMA Band 6.

These observations were intended to provide snapshots of these disks.¹⁷ Due to the short on-source time (~ 15 minutes), the peak signal-to-noise ratio (S/N) for each source ranges from 5 to 20. We attempted one round of phase-only self-calibration on sources 2M0412, 2M0434, and 2M0450. For 2M0436 and 2M0508, the emission morphology was largely altered after self-calibration, so we did not apply the solutions. CIDA 12 has too low S/N to improve from self-calibration. The self-calibration solutions are not applied to CO line emission channels, since the improvement is negligible.

The continuum images were generated using the `ttclean` task with multiscale imaging, with the Briggs `robust` weighting parameters being 0.5 for 2M0434, 2M0436, 2M0450, and 2M0508; 1 for 2M0412; and 2 for

CIDA 12. The adopted weighting parameters are compromises between resolution and sensitivity. The uv coverage of observations produced elongated beams (aspect ratio ~ 2). For better visualization, we performed uv -tapering to get more circular beams. Images with original beams and uv -tapered beams are shown in Figure 1. The beam sizes are $0''.03$ – $0''.07$, and the rms noise is 30–40 mJy beam $^{-1}$, with detailed values summarized in Table 2.

For line images, after subtracting the continuum emission using the `uvcontsub` task, we applied uv -tapering to enhance the S/N of the line images. The beams are tapered to $0''.2$ for 2M0412 and 2M0434 and $0''.1$ for the other four targets. We detected (or marginally detected) ^{12}CO for all six targets and ^{13}CO for 2M0412 and 2M0434. The channel maps in velocity and moment maps of detected ^{12}CO and ^{13}CO are shown in Appendix A.

3. Results

From our ALMA observations, four disks in the sample show rings and cavities in their dust emission, while the other two show compact smooth emission. In this section, we characterize the dust emission through fitting the directly observable visibilities and present the measurement of dust and gas disk properties.

3.1. Visibility Fitting of Dust Morphology

The peak fluxes of our disks range from 0.19 to 0.47 mJy beam $^{-1}$, which corresponds to peak S/Ns of about 6–12 from the non- uv -tapered images in Figure 1. Dust emission from these disks is faint, as expected for low-mass M stars. To quantify the dust emission morphology without biases introduced by the image reconstruction, we fit the brightness profiles in the visibility domain. The model profiles are selected based on eye identification of disk substructures. For 2M0450 and CIDA 12, the function to describe their deprojected brightness is a centrally peaked axisymmetric Gaussian profile:

$$I_{\text{GP}}(r) = 10^f \exp\left(-\frac{r^2}{2\sigma^2}\right) \quad (1)$$

where $I_{\text{GP}}(r)$ is the Gaussian brightness profile as a function of disk radius r , with 10^f and σ being the amplitude and Gaussian width, respectively. For the other four disks showing cavities and rings, we modeled their morphologies with a radially asymmetric Gaussian ring whose inner and outer width can

¹⁷ Young M stars can happen to be active in millimeter wavelength in timescale of minutes (e.g., MacGregor et al. 2018; Mairs et al. 2019), which would be an issue for disk analysis, especially for compact sources like 2M0450 and CIDA 12. After performing time-series measurement of the fluxes for 2M0450 and CIDA 12, no significant flux variations are found during our observations.

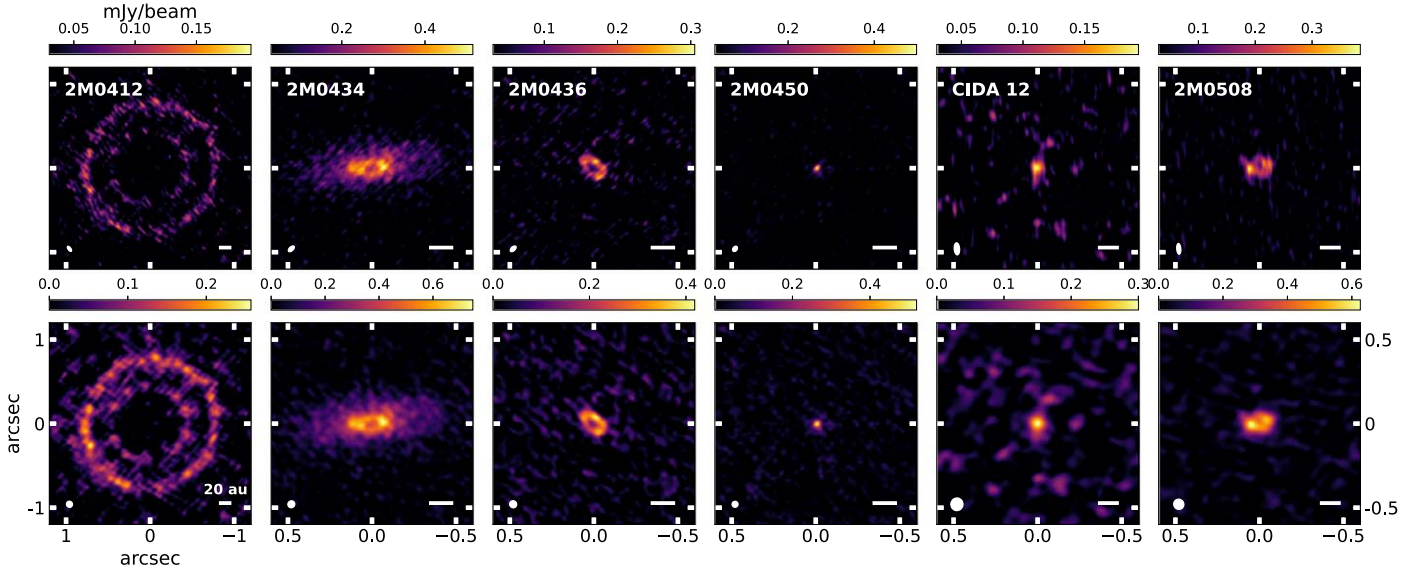


Figure 1. The top panels show ALMA continuum images of disks around mid-M stars in Taurus at 1.3 mm. The box size for 2M0412 is $2''4$, and the size for the rest is $1''2$. The white scale bars represent 20 au. The bottom panels are for the same targets with beams tapered to a more circular shape for better visualization. The beam sizes and rms noise of each image are detailed in Table 2.

differ:

$$I_{\text{AGR}} = \begin{cases} 10^f \exp\left(-\frac{(r - r_{\text{peak}})^2}{2\sigma_1^2}\right) & (r \leq r_{\text{peak}}) \\ 10^f \exp\left(-\frac{(r - r_{\text{peak}})^2}{2\sigma_2^2}\right) & (r > r_{\text{peak}}) \end{cases}, \quad (2)$$

where 10^f , r_{peak} , and σ_i are the amplitude, peak location, and ring width, respectively, for the inner and outer side. A radially asymmetric Gaussian ring has been previously used to describe the rings in transition disks (e.g., Pinilla et al. 2017a, 2018; Huang et al. 2020; Kurtovic et al. 2021). This model fitting is motivated by the accumulation of dust particles trapped in radial pressure bumps (Pinilla et al. 2017a). Dust particles in the outer disk are expected to take a longer time to grow and drift radially toward the pressure bump. Hence, the external width of the ring is expected to be larger than the internal width (e.g., Figure 4 in Pinilla et al. 2015).

Using the adopted radial profiles, we first generate corresponding face-on images. Each model image is projected with an inclination (i) and a position angle (PA) and combined with a spatial offset ($\delta_{\text{R.A.}}$, $\delta_{\text{decl.}}$), which adds another four parameters. We generate each model image with a pixel size of 3 mas, which is far smaller than our synthesized beam (~ 40 mas). We then use `galario` (Tazzari et al. 2018) to transform each model image into complex visibilities sampled at the same (u, v) points as those in the observations and calculate the $\chi^2 = \sum_k w_k |V_{\text{obs}}(u_k, v_k) - V_{\text{mod}}(u_k, v_k)|^2$, where w_k is the observed visibility weight; the likelihood function is then calculated as $L \propto \exp(-\chi^2/2)$. We assumed a uniform prior probability distribution for the parameters above (for inclination the probability $\propto \sin i$ to get a uniform disk orientation).

We sample the posterior probability distribution using a Markov Chain Monte Carlo (MCMC) method (`emcee`; Foreman-Mackey et al. 2013) with 50 walkers and 10,000 steps. After running MCMC, we get posterior samples after 10 times the integrated autocorrelation time to ensure stationary

posterior samples. Results for each model parameter are shown in Table 3, with the reference values adopted as the median values of posterior samples and their uncertainties estimated from the 16th and 84th percentiles. The comparisons between observations and models in the visibility plane, the image plane, and deprojected azimuthally averaged radial profiles are shown in Figure 2. The brightness profiles of each model are shown in Figure 3. All best-fit model images show reasonable matches with observations, with no residuals above 5σ .

3.2. Rings and Cavities

3.2.1. Disks with Substructures in Images

As mentioned in Section 3.1, rings are modeled as radially asymmetric Gaussian rings. Our results show that the rings generally have wider outer width than inner width, while 2M0436 shows the opposite. Here we summarize the peak locations and Gaussian σ widths from the best-fit models.

2M0412 has the largest rings and cavity in the sample, with the inner ring peak at 61.7 au and the outer ring peak at 113.9 au. The inner ring has an inner width of 0.9 au and outer width of 17.5 au, while the outer ring has 5.5 au inner side and 9.5 au outer side. For the ratios between the ring outer width and inner width, the best-fit model gives 19.8 for the inner ring and 1.7 for the outer ring. The outer ring is brighter than the inner ring, with the outer peak intensity 2.1 times as large as that of the inner peak. The brightness ratio between the first ring and the exterior gap is around 6.8.

For 2M0434, we find a ring peak at 9.8 au, followed by radially extended emission beyond the ring. The ring has 1.5 au inner width and 8.2 au outer width. A Gaussian profile in Section 3.1 fits the outer broad emission well. For 2M0508, the best model finds a ring peak at 6.8 au, where its inner width is 0.8 au and outer width is 7.1 au. In 2M0436, the best-fit ring peaks at 12.2 au, with an outer width being 1.0 au and a larger inner width being 4.7 au, showing different ring width behavior.

Some potential asymmetries appear in the images. For example, the northern part of 2M0434 seems to be brighter than its southern part as shown by the residual map, and a bright

Table 3
Dust Disk Model Parameters from uv Modeling

Source Name Model	2M0412 2AGR	2M0434 GP&AGR	2M0436 AGR	2M0450 GP	CIDA 12 GP	2M0508 AGR	Unit
f_1	$8.63^{+0.03}_{-0.03}$	$9.83^{+0.01}_{-0.01}$	$9.98^{+0.03}_{-0.03}$	$10.45^{+0.05}_{-0.05}$	$9.54^{+0.09}_{-0.08}$	$9.93^{+0.03}_{-0.03}$	$\log_{10} \text{ Jy sr}^{-1}$
$r_{\text{peak},1}$	$415.10^{+8.71}_{-6.41}$...	$84.68^{+6.05}_{-7.35}$	$39.80^{+6.38}_{-4.54}$	mas
σ_{11}	$5.93^{+6.51}_{-4.21}$	$268.38^{+3.04}_{-3.02}$	$32.90^{+5.84}_{-6.23}$	$16.89^{+1.44}_{-1.28}$	$54.06^{+11.11}_{-11.15}$	$4.69^{+5.94}_{-3.47}$	mas
σ_{12}	$117.71^{+13.71}_{-11.45}$...	$6.88^{+5.34}_{-4.63}$	$41.91^{+3.61}_{-4.01}$	mas
f_2	$8.96^{+0.02}_{-0.02}$	$9.95^{+0.03}_{-0.03}$	$\log_{10} \text{ Jy sr}^{-1}$
$r_{\text{peak},2}$	$766.27^{+7.44}_{-14.94}$	$67.41^{+8.91}_{-7.60}$	mas
σ_{21}	$37.05^{+7.31}_{-12.02}$	$10.15^{+7.94}_{-6.71}$	mas
σ_{22}	$63.74^{+8.73}_{-5.68}$	$56.22^{+4.81}_{-5.52}$	mas
Inc	$15.90^{+0.70}_{-0.82}$	$68.54^{+0.23}_{-0.23}$	$53.46^{+1.41}_{-1.49}$	$43.26^{+7.84}_{-10.37}$	$65.53^{+7.43}_{-12.65}$	$54.34^{+1.67}_{-1.78}$	deg
PA	$124.14^{+2.81}_{-2.06}$	$96.67^{+0.24}_{-0.24}$	$46.96^{+2.03}_{-2.05}$	$63.01^{+12.43}_{-12.87}$	$169.94^{+5.22}_{-6.59}$	$98.90^{+2.10}_{-2.10}$	deg
$\Delta_{\text{R.A.}}$	$2.77^{+1.86}_{-2.06}$	$10.89^{+1.03}_{-1.05}$	$7.86^{+1.12}_{-1.15}$	$-3.13^{+0.96}_{-0.97}$	$9.05^{+3.21}_{-3.30}$	$12.36^{+1.38}_{-1.40}$	mas
$\Delta_{\text{decl.}}$	$-0.69^{+2.11}_{-2.12}$	$10.37^{+0.50}_{-0.49}$	$5.76^{+1.11}_{-1.11}$	$-8.98^{+0.91}_{-0.92}$	$-2.15^{+6.02}_{-6.18}$	$5.77^{+1.10}_{-1.12}$	mas
$F_{1.3 \text{ mm}}$	$17.58^{+0.33}_{-0.32}$	$30.73^{+0.26}_{-0.24}$	$2.71^{+0.05}_{-0.05}$	$0.85^{+0.03}_{-0.03}$	$0.60^{+0.06}_{-0.06}$	$3.02^{+0.09}_{-0.09}$	mJy
M_{dust}	$11.50^{+1.15}_{-1.15}$	$19.31^{+1.93}_{-1.93}$	$1.68^{+0.17}_{-0.17}$	$0.53^{+0.05}_{-0.05}$	$0.51^{+0.05}_{-0.05}$	$2.61^{+0.26}_{-0.26}$	M_{\oplus}
$R_{68\%}$	$118.0^{+0.5}_{-0.3}$	$55.1^{+0.5}_{-0.5}$	$11.8^{+0.2}_{-0.2}$	$3.6^{+0.3}_{-0.3}$	$13.8^{+2.8}_{-2.9}$	$15.6^{+0.5}_{-0.5}$	au
$R_{90\%}$	$126.0^{+0.9}_{-0.6}$	$81.2^{+0.8}_{-0.8}$	$13.2^{+0.4}_{-0.3}$	$5.1^{+0.5}_{-0.4}$	$19.6^{+4.0}_{-4.1}$	$20.4^{+0.8}_{-0.8}$	au

Note. Model row: AGR for asymmetric Gaussian ring, GP for Gaussian profile.

spot appears at the northwest of 2M0436, which are both at 3σ levels. The west part of 2M0508 is brighter, though the significance is less than 3σ level. Deeper observations are necessary to check whether the above potential asymmetries exist or not. In this work, we focus on only axisymmetric substructures.

3.2.2. Potential Cavities around 2M0450 and CIDA 12

Gaussian profiles (Equation (1)) can only describe continuous disks with a monotonically decreasing radial profile. The Nuker profile, which was first introduced to describe the brightness profiles of elliptical galaxies (Lauer et al. 1995), can also reproduce ringlike emission with a central depression. The Nuker profile is formulated as

$$I_{\nu}(r) = 10^f \left(\frac{r}{r_t} \right)^{-\gamma} \left[1 + \left(\frac{r}{r_t} \right)^{\alpha} \right]^{(\gamma-\beta)/\alpha}, \quad (3)$$

where r_t is the transition radius, α is the transition index, β is the outer disk index, and γ is the inner disk index. The Nuker profile behaves as $r^{-\gamma}$ at $r \ll r_t$ and $r^{-\beta}$ at $r \gg r_t$. The transition index α determines how smooth/sharp the transition is between these two asymptotic behaviors (see Figure 2 in Tripathi et al. 2017). With $\beta > 0$ and $\gamma < 0$ the Nuker profile can describe a ringlike morphology.

Appendix C presents the detailed modeling with Nuker profiles on 2M0450 and CIDA 12. Interestingly, the best-fit Nuker profiles for the two smooth-appearing disks show depleted inner emission with emission peak at ~ 1.7 au for 2M0450 and 5.7 au for CIDA 12 (see Figure C1).

However, the Nuker profile has more parameters than the Gaussian profile, which results in a larger Bayesian Information Criterion (BIC)¹⁸ value. Hence, we still treat 2M0450 and

CIDA 12 as nonstructured disks in this work. Future higher angular resolution observations are needed to check their potential small cavities.

3.3. Potential Unresolved Central Emission in 2M0436

2M0436 shows a ring with a wider inner width, which is contrary to models of dust trapping in pressure bumps. One possibility is that an external object has truncated the outer disk, which we expect to be substellar since no stellar companions have been detected (Kraus et al. 2011; Kraus & Hillenbrand 2012). Constraining the mass of the substellar object given current knowledge would be highly uncertain and beyond the scope of this work. Other possibilities are the presence of central compact emission blending with the ring emission and the blending of multiple unresolved rings. Compact emission at the center is also hinted at because the model intensity of 2M0436 slightly underpredicts the emission of the very inner disk (right column in Figure 2), though this difference is not statistically significant. An example is CIDA 1, where a model considering only one ring results in a ring with wider inner width (Kurtovic et al. 2021), while higher angular resolution observations reveal a compact inner disk and the inclusion of an inner disk recovers a ring with wider outer width (Pinilla et al. 2021).

In Appendix B, we show the results of modeling 2M0436 with a ring and a central point. The flux of the added central point emission is $0.04^{+0.03}_{-0.03}$ mJy (corner plot statistics in Figure B2). The new radial profile increases the inner emission and matches the observations better than a ring-only model, while the ring still displays a wider inner width after including a point emission. However, the result of modeling with central point emission could be limited by current observations; deeper sensitivity and higher angular resolution are necessary for future observations.

3.4. Dust Disk Millimeter Flux, Mass, and Size

The millimeter fluxes, masses, and sizes of the dust disk are not explicit parameters in the models and are inferred from

¹⁸ The BIC is a criterion for the preference of models. It is defined as $\text{BIC} = k \ln(n) - 2 \ln(\hat{L})$, where k is the number of model parameters, n is the number of data points, and \hat{L} is the maximized value of the likelihood function.

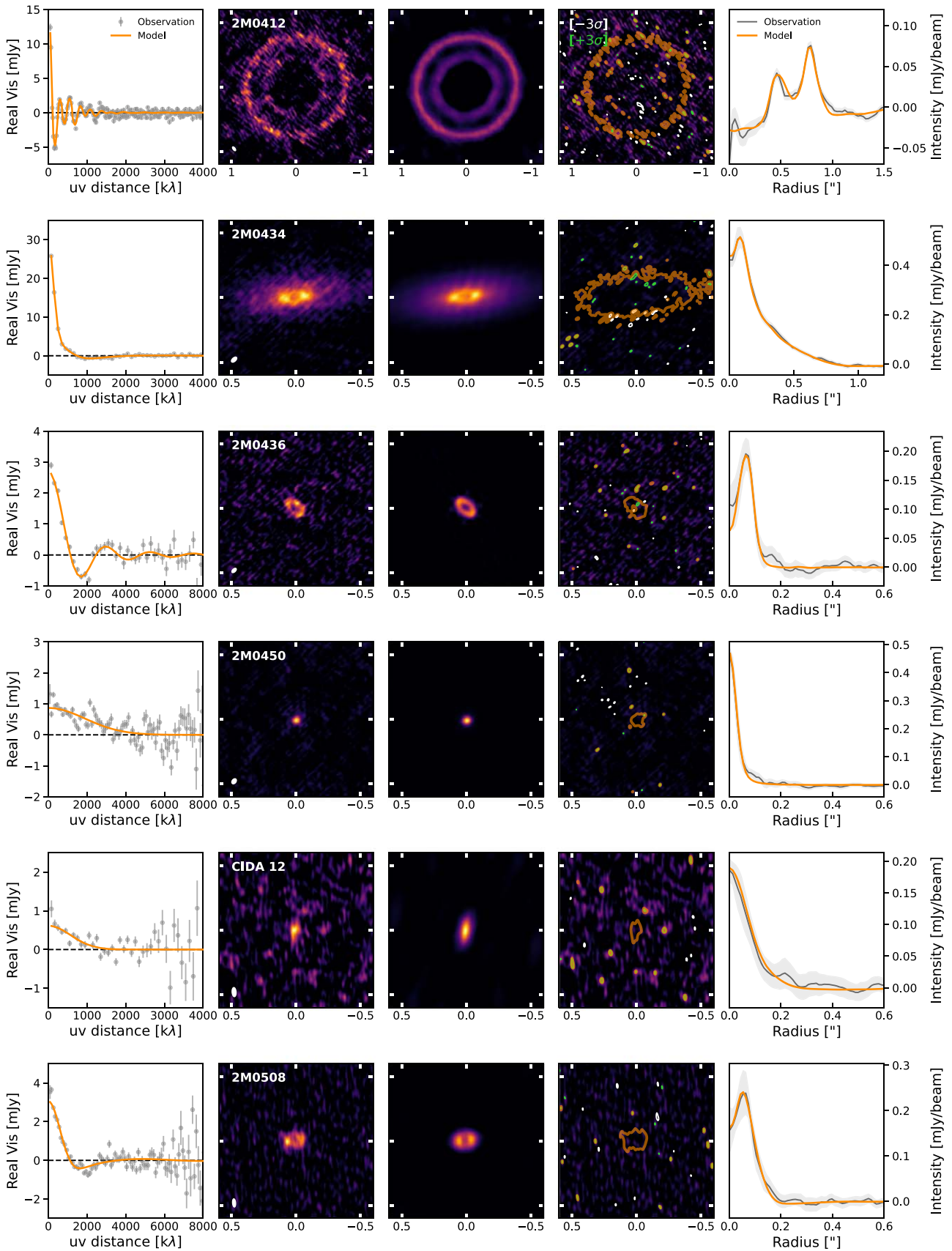


Figure 2. Best-fit visibility fitting results vs. observations. Columns from left to right: (1) the real part of deprojected and binned visibilities from observations and best-fit models; (2) observational continuum images; (3) model images convolved with the same beam as observations; (4) residual images, with white contours at -3σ and green contours at 3σ , and overlaid orange contours are from continuum images at the 3σ level; (5) azimuthally averaged radial profiles for observations and convolved model images, where light-gray shaded regions represent the standard deviation at each radial bin divided by the square root of the number of beams in the radial bin.

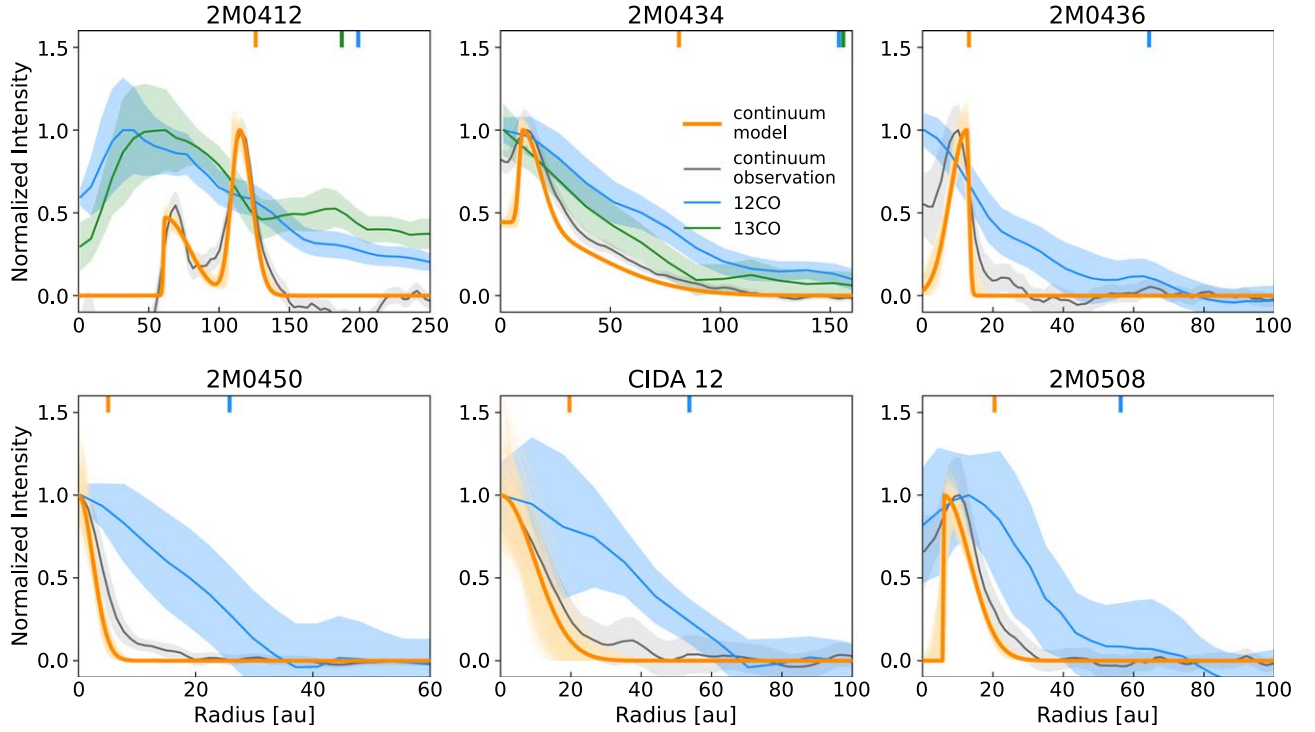


Figure 3. Normalized radial profiles of dust continuum, ^{12}CO and ^{13}CO (if detected). The thick orange curves are the best-fit model profiles of dust continuum (i.e., unconvolved); the thin light-orange lines correspond to 1000 randomly selected model intensities from the posterior sample (Section 3.1). The gray lines are radial profiles of dust continuum from observations. The blue and green curves correspond to ^{12}CO and ^{13}CO azimuthally averaged radial profiles retrieved from moment 0 images, respectively, except for 2M0412, where moment-8 images are used owing to severe cloud contamination. The colored regions represent 1σ uncertainty for each radial profile. The ticks at the top of each panel represent the radius enclosing 90% emission of each profile, with orange for dust continuum, blue for ^{12}CO , and green for ^{13}CO .

fitting results. Since our models are axisymmetric, the total fluxes are obtained through $F_\nu = f_i(\infty)$, where $f_i(r)$ is the flux within radius r :

$$f_\nu(r) = 2\pi \int_0^r I_\nu(r') r' dr'. \quad (4)$$

The dust disk sizes are defined to be a radius that encloses 68% and 90% of total fluxes, consistent with choices from previous studies (see, e.g., the review by Miotello et al. 2023). The continuum fluxes, sizes, and their uncertainties are then computed from the last 5000 steps of the chains, as shown in Table 3. Most adopted models reproduce lower fluxes than those seen at short baselines (left column in Figure 2), likely due to the fact that either large-scale emission is resolved out by high angular resolution beams or faint emission is buried by the noise, so that we lack extra components in our modeling that could account for the flux difference between models and observations. Future observations with deeper sensitivity and shorter baselines are needed to fix this issue.

For CIDA 12, Nuker profiles reproduce millimeter flux better than that from Gaussian profiles. The visibility near zero-spacing baselines indicates that its flux is above 1 mJy, and it is consistent with $1.16^{+0.09}_{-0.09}$ mJy reported in Akeson et al. (2019), specifically the Gaussian profile gives $0.60^{+0.06}_{-0.06}$ mJy, while the Nuker profile recovers a flux of $1.20^{+0.98}_{-0.51}$ mJy.

Under the assumption that the dust disk is optically thin at millimeter wavelengths, the dust disk mass M_{dust} is estimated

following Hildebrand (1983) as

$$M_{\text{dust}} \approx \frac{D^2 F_\nu}{\kappa_\nu B_\nu(T_{\text{dust}})}, \quad (5)$$

where D is distance from Gaia DR3 (Gaia Collaboration et al. 2023), κ_ν is dust opacity for which we adopt a power law of $\kappa_\nu = 2.3 \text{ cm}^2 \text{ g}^{-1} (\nu/230 \text{ GHz})^{0.4}$ (Andrews et al. 2013), and B_ν is the Planck function where the T_{dust} is assumed at 20 K (e.g., Ansdell et al. 2016).

We assume 10% uncertainty in the source flux calibration (Diaz Trigo et al. 2019; see also Francis et al. 2020) to calculate the dust mass uncertainty. Table 3 summarizes the estimated dust masses. 2M0434 has the most massive disk in our sample, with a dust mass $19.31^{+1.93}_{-1.93} M_\oplus$, while CIDA 12 has the lowest dust mass with only $0.51^{+0.05}_{-0.05} M_\oplus$. We note that these dust masses serve as lower limits, since part of the disk could be optically thick in reality (see Section 4.1 for a brief calculation). The assumed dust temperature would also affect the estimated dust mass: for example, the dust mass would be higher/lower by $\sim 40\%/50\%$ if the actual averaged dust temperature is 15 K/30 K.

3.5. CO Emission

Gas disk observations and comparisons to dust disks are helpful to understand disk evolution as a whole. To compute the integrated fluxes of CO lines, extraction regions need to be determined. We first generate the cumulative flux distributions and determine the radii where CO emission no longer increases. Then, we draw circular regions as large as these

Table 4
Measurement of Gas Emission from CO Isotopes

Molecule	Integrated Flux (Jy km s ⁻¹)	Peak Intensity (mJy beam ⁻¹ km s ⁻¹)	Velocity Range (km s ⁻¹)	Chan. Width (km s ⁻¹)	Chan. rms (mJy beam ⁻¹)	Beam (mas × mas, deg)	R _{90%} (au)	R _{gas} /R _{dust}
2M0412								
¹² CO	1.08 ± 0.06	71.4	4.0–8.0	0.4	5.5	215 × 209, –3	≥198.9	≥1.6
¹³ CO	0.54 ± 0.06	39.2	4.0–8.0	0.4	5.8	220 × 212, –2	≥187.2	≥1.5
C ¹⁸ O	<0.15	...	4.0–8.0	0.4	4.2	222 × 211, 5
2M0434								
¹² CO	1.21 ± 0.11	130.5	2.0–10.0	0.4	6.9	209 × 175, –67	≥153.9	≥1.9
¹³ CO	0.61 ± 0.09	74.2	2.0–10.0	1.0	4.4	170 × 159, –57	≥155.9	≥1.9
C ¹⁸ O	<0.21	...	2.0–10.0	1.0	3.4	169 × 159, –55
2M0436								
¹² CO	0.38 ± 0.07	56.1	1.4–9.4	0.8	3.5	112 × 99, –51	≥64.4	≥4.9
¹³ CO	<0.24	...	1.4–9.4	0.8	3.8	113 × 100, –55
C ¹⁸ O	<0.17	...	1.4–9.4	0.8	2.9	113 × 101, –54
2M0450								
¹² CO	0.10 ± 0.04	30.3	2.0–12.0	1.0	2.6	110 × 97, –77	≥25.8	≥5.1
¹³ CO	<0.11	...	2.0–12.0	1.0	2.9	112 × 98, –82
C ¹⁸ O	<0.10	...	2.0–12.0	1.0	2.2	111 × 99, –85
CIDA 12								
¹² CO	0.24 ± 0.05	57.6	2.0–12.0	1.0	3.0	101 × 94, –37	≥53.7	≥2.7
¹³ CO	<0.15	...	2.0–12.0	1.0	3.3	102 × 96, –40
C ¹⁸ O	<0.12	...	2.0–12.0	1.0	2.5	101 × 97, –35
2M0508								
¹² CO	0.19 ± 0.06	39.6	2.0–12.0	1.0	2.9	100 × 93, –39	≥56.3	≥2.8
¹³ CO	<0.20	...	2.0–12.0	1.0	3.3	101 × 96, –43
C ¹⁸ O	<0.19	...	2.0–12.0	1.0	2.5	101 × 97, –38

radii and project the regions with the same inclination and PA as those of dust disks. CO fluxes are then retrieved from these elliptical regions. The uncertainties of the integrated flux are measured in nonemission channels with the same velocity range as those used to generate moment 0 images, as the standard deviation of integrated fluxes estimated from 1000 randomly distributed elliptical regions with the same shape as the above extraction regions. The fluxes and uncertainties of ¹²CO, ¹³CO, and C¹⁸O $J = 2-1$ lines are listed in Table 4, as well as the 3σ upper limits for the nondetections.

We detect (S/Ns of integrated fluxes above 3σ) ¹²CO in five disks and ¹³CO in 2M0412 and 2M0434. 2M0450 has a marginal detection of ¹²CO with an S/N of 2.7σ . The gas disk sizes are measured the same way as dust disk sizes, adopting the same inclination and PAs from the fits to the dust continuum emission. 2M0450 has the smallest gas disk, about 26 au, while 2M0412 has the largest gas disk, about 199 au. When compared to dust disk sizes, the ratio ranges from 1.6 (2M0412) to 5.1 (2M0450). Since the largest angular scale recovered by our observations is only $\sim 0''.6$, the gas emission at large radii is likely resolved out; cloud absorption could also result in underestimation of disk sizes (e.g., Long et al. 2022); by 10%–30% with a typical cloud emission line width of 1–2 km s⁻¹, we treat the gas radii $R_{\text{gas},90\%}$ as lower limits. The measured gas disk sizes and size ratios compared to dust disks are summarized in Table 4.

Figure 3 shows the azimuthally averaged radial profiles of gas emission and the best-fit continuum model intensity profiles. CO emission around 2M0412 suffers from severe cloud absorption, so we show the profile extracted from the moment 8 map¹⁹ instead. Among the six disks, 2M0412 shows

a drop in emission inside the dust cavity, with peak emission located at ~ 36 au for ¹²CO and 54 au for ¹³CO. The cloud absorption may affect these values. A tentative drop of ¹²CO is seen around 2M0508, with the peak location overlapping with the dust cavity size. No other clear evidence of gas emission depletion is found in the other four disks, under current $\sim 0''.1$ ($0''.2$ for 2M0434) resolution for gas images.

4. Discussion

Among the six disks, the four brighter disks show cavity and ring substructures and the two faintest disks appear as smooth emission. The cavities can be large, up to 60 au, while the most common sizes are about 10 au. For the two smooth disks, visibility fitting suggests the possibility of them harboring cavities down to 2 au. Comparing the gas disks with dust disks, two disks show large size ratios of about 5. With these results, we organize our discussions as follows: In Section 4.1, we discuss the disk global properties in the context of disk evolution. Section 4.2 focuses on the detected substructures at millimeter wavelength and spectral energy distribution (SED) hints for cavities for micron-sized dust disk. Finally, we discuss the mechanisms that are possibly responsible for the observed rings and cavities in Section 4.3.

4.1. Context with Disk Evolution

Putting disk properties together with the disk population can help constrain global disk evolution (Manara et al. 2023). Previous studies have shown that the millimeter luminosity of disks scales with stellar mass (e.g., Andrews et al. 2013; Ansdell et al. 2016, 2017; Barenfeld et al. 2016; Pascucci et al. 2016). The left panel of Figure 4 compares the six disks in this

¹⁹ Moment 8 map represents the maximum value along the spectrum.

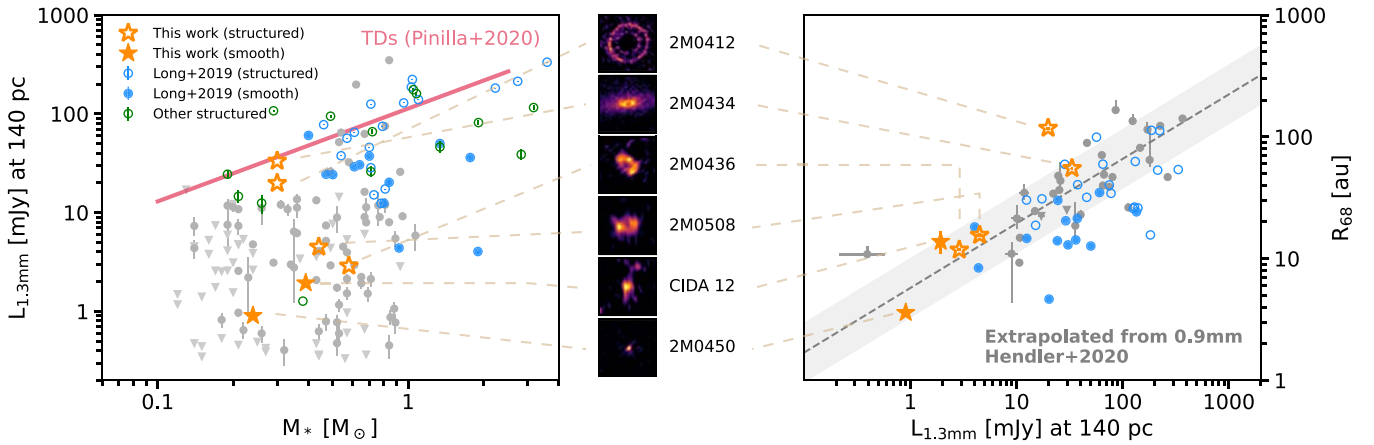


Figure 4. Scaling relations for Taurus disks. Left: millimeter luminosity at 1.3 mm vs. stellar mass. Open orange stars are structured disks, and filled orange stars are smooth disks in this work. Blue circles are for disks in Long et al. (2019), with open ones for structured disks and filled ones for smooth disks. Open green circles represent other structured disks in the literature (see references in text). The gray circles (detection) and triangles (upper limits) are other Taurus disks (Manara et al. 2023). The light-pink line is the scaling relation fitted to disks with large cavities (>20 au) from Pinilla et al. (2020). Middle: thumbnails of each target’s continuum image; the box sizes are varied so that the targets are shown clearly. Right: dust disk size $R_{\text{dust},68\%}$ vs. millimeter luminosity. The orange stars are the same as in the left panel; blue circles are from Long et al. (2019), with open and filled ones for structured and smooth disks, respectively; and gray circles are from Tripathi et al. (2017) and Kurtovic et al. (2021). The scaling relation is from Hendler et al. (2020). The gray circles and the scaling relation are extrapolated from observations at ALMA Band 7 (~ 0.9 mm).

work with other Taurus disks with detected substructures in the $L_{\text{mm}}-M_*$ plane (Long et al. 2018; Hashimoto et al. 2021; Kurtovic et al. 2021; Yamaguchi et al. 2021; Jennings et al. 2022; Zhang et al. 2023; review by Bae et al. 2023), as well as with other Taurus disks from Manara et al. (2023). The properties of the six disks follow the correlation for the whole Taurus population (Andrews et al. 2013). The four structured disks are brighter than the two smooth disks. It could be that the two smooth disks simply formed with less dust, while it could also be due to the lack of substructures to trap the dust and prevent dust from drifting toward the star. However, if the potential small cavities shown in Section 3.2.2 are indeed present in 2M0450 and CIDA 12, either their trapping efficiency is lower or the formation time of dust traps is later than the brighter disks.

If disks are optically thick, the low L_{mm} might not correspond to a low dust mass. To have a simple estimate of the optical depth for the two smooth disks, we estimate the disk midplane temperature following Huang et al. (2018a):

$$T_{\text{mid}}(r) = \left(\frac{\phi_{\text{fl}} L_*}{8\pi r^2 \sigma_{\text{SB}}} \right)^{1/4}, \quad (6)$$

where σ_{SB} is the Stefan–Boltzmann constant and ϕ_{fl} is the disk flaring angle. A conservative $\phi_{\text{fl}} = 0.02$ is used (Huang et al. 2018a). Then, the optical depth τ_{ν} is calculated using

$$I_{\nu}(r) = B_{\nu}(T_{\text{mid}}(r))(1 - \exp(-\tau_{\nu}(r))), \quad (7)$$

where B_{ν} is Planck’s law for blackbody radiation. The conservatively estimated peak τ is ~ 0.5 for 2M0450 and 0.15 for CIDA 12, so that 2M0450 is partially optically thick and CIDA 12 is nearly optically thin. We expect the above arguments regarding dust trapping to hold for CIDA 12 at least.

The $L_{\text{mm}}-M_*$ relation has been suggested to be flatter for disks with inner cavities (Pinilla et al. 2018, 2020; pink line in left panel of Figure 4). However, those studies lack data for the very low mass stars and disks with small cavities (<20 au). Furthermore, the flatter relation is not observed in any individual star-forming region. The two fainter disks with

small inner cavities (2M0436 and 2M0508) deviate significantly from this flatter relation. Conservative estimates of their optical depth yield maximum values of 0.6 for 2M0436 and 0.5 for 2M0508, suggesting that the two disks are partially optically thick. Boulder formation could also lower the observable millimeter flux (Pinilla et al. 2020). A combination of optical thickness and boulder formation in these disks might explain their deviation.

In addition to stellar mass, the millimeter luminosity also scales with disk size (Tripathi et al. 2017; Andrews et al. 2018b). The right panel of Figure 4 compares the six disks in this work with other Taurus disks (Tripathi et al. 2017; Long et al. 2019; Kurtovic et al. 2021) in the $R_{\text{eff}}-L_{\text{mm}}$ plane with the best-fit scaling relation $R_{\text{eff}} \propto L_{\text{mm}}^{0.53 \pm 0.12}$ from Hendler et al. (2020).²⁰ Numerical simulations have shown that disks fall along the observed relation $L_{\text{mm}} \propto R_{\text{eff}}^2$ if disks are in the radial-drift-dominated regime, while for disks with strong substructures they follow a relation of $L_{\text{mm}} \propto R_{\text{eff}}^{5/4}$ (Rosotti et al. 2019; Zormpas et al. 2022). The two relations intersect at the top end of the size–luminosity relation (i.e., for bright and large disks; Zormpas et al. 2022).

Most of our six disks follow the observed relation $L_{\text{mm}} \propto R_{\text{eff}}^2$, except 2M0412, whose large size stands out at its luminosity regime, suggesting that a pressure bump was built early at large disk radii of 2M0412 (Long et al. 2023). 2M0436, 2M0450, CIDA 12, and 2M0508 fall at the faint end of the $L_{\text{mm}} \propto R_{\text{eff}}^2$ relation and hence are likely drift dominated. For the structured 2M0436 and 2M0508, either their substructures are too weak to retain the dust in their rings or their rings formed late when the disks have already evolved to the faint end of the $L_{\text{mm}} \propto R_{\text{eff}}^2$ relation.

The gas disk is universally found to be more extended than the dust disk (e.g., Barenfeld et al. 2017; Ansdell et al. 2018; Long et al. 2022). In our six disks, we find that the two largest dust disks (2M0412 and 2M0434) have an $R_{90,\text{gas}}/R_{90,\text{dust}}$ of

²⁰ Fluxes of sources in Kurtovic et al. (2021) and the scaling relation in Hendler et al. (2020) are extrapolated from 0.9 to 1.3 mm using a spectral index of 2.2 (Andrews 2020); the slopes of the scaling relation at these two wavelengths are found to be identical (Tazzari et al. 2021).

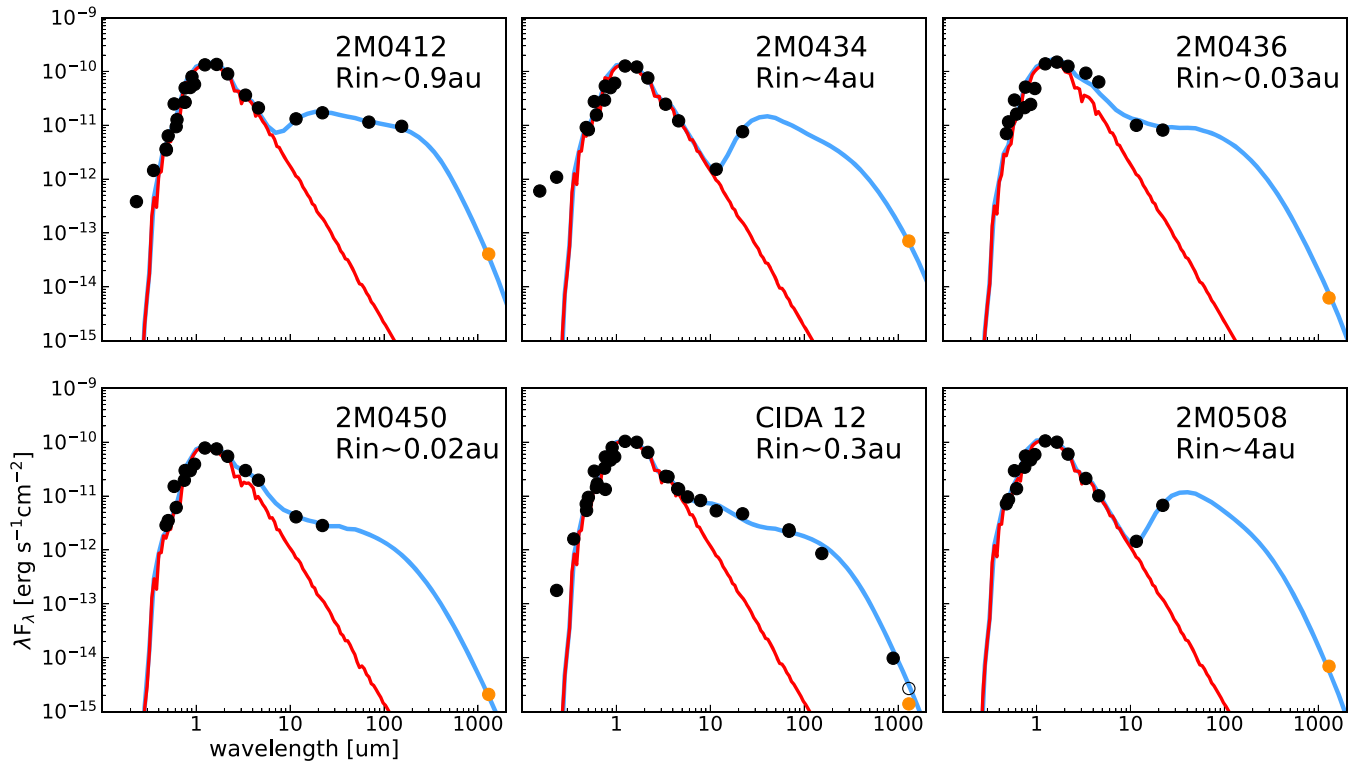


Figure 5. SEDs from observations (black circles) and radiative transfer modeling (blue lines). The red lines are the stellar photospheric emission applied with extinction. The orange circles are measurements at 1.3 mm in this work; for CIDA 12 the open black circle represents the 1.3 mm flux from Akeson et al. (2019). R_{in} in the upper right corner of each panel are cavity sizes from radiative transfer modeling for micron-sized dust grains.

~ 1.5 and 1.9 , respectively. CIDA 12 and 2M0508 have a ratio of ~ 2.7 . The two smallest dust disks (2M0436 and 2M0450) have the most extreme ratios of around 5, which are also among the largest values for the disk population (Long et al. 2022). Early formation of pressure bumps in the two largest dust disks 2M0412 and 2M0434 may explain their lower size ratios. 2M0412 shows a large ring at large radii of 114 au, while 2M0434’s ring peaks at about 10 au, which is far smaller than its size of 81 au, indicating that its extended emission outside the ring holds unresolved substructures. Trapman et al. (2019) suggest that disks with $R_{90,gas}/R_{90,dust} > 4$ can only be explained with dust evolution and radial drift. This is likely what 2M0436 and 2M0450 have undergone owing to their such extreme size ratios, which is also consistent with more efficient dust radial drift expected in lower-mass stars (Pinilla et al. 2013). These size ratios should be considered as lower limits since they are affected by cloud absorption and the observations lack short-spacing data (see the figures in Appendix A); hence, the gas emission is probably not recovered as well as dust emission.

4.2. Substructures in Disks around Mid- to Late M Stars

Current studies of substructures mostly come from disks around solar-like stars (e.g., Andrews et al. 2018a; Long et al. 2018; Cieza et al. 2021). Van der Marel & Mulders (2021) found that substructures are less common around M stars, which was mostly based on studies with intermediate spatial resolution (~ 25 au in radius) and biased toward larger disks, while detecting substructures around M stars needs higher resolution since they are smaller. Currently only a few disks around M stars (especially mid- to late type) have been imaged at high spatial resolution. In Taurus, Kurtovic et al. (2021)

surveyed at a resolution of $\sim 0''.1$ (14 au) for a sample of six disks around M4–M5 stars and found two disks with a cavity and one ringed disk. The sample in Kurtovic et al. (2021) is biased to the brightest disks in the corresponding stellar regime and hence favorable for substructure detection. Hashimoto et al. (2021) reported an asymmetric dust ring around a cavity around the M4.5 star ZZ Tau IRS with resolution $\sim 0''.2$. Other studies toward the Lupus and Ophiuchus regions have also detected a few structured disks around mid- to late M stars with resolutions down to ~ 4 au (González-Ruilova et al. 2020; Cieza et al. 2021; van der Marel et al. 2022).

Cavity+ring seems to be the most common substructure around low-mass stars. In our sample, substructures are detected in four (2M0412, 2M0434, 2M0436, and 2M0508) of six disks. The substructures we identify are all cavities surrounded by rings, with varying numbers in individual disks. Combined with structured disks around very low mass stars collected in Pinilla (2022), the cavity frequency seems higher than that around solar-like stars. Taking disks in Taurus as an example (Hashimoto et al. 2021; Kurtovic et al. 2021; this work), high spatial resolution imaging revealed 7 disks with cavities out of 13 disks around M3–M6 stars. In comparison to stars earlier than M3 in Taurus, only 4 out of 32 disks analyzed by Long et al. (2019) show cavities (5/32 considering the reanalysis in Zhang et al. 2023). However, the sample around mid- to late M stars used here might be more biased than that in Long et al. (2019). Based on SED modeling (see below and Figure 5), two out of the six disks in this work have cavities > 1 au, which is higher than the transition disk fraction of $\sim 8\%$ within the full Class II disks (van der Marel et al. 2016; similar fraction is obtained when limiting to M3–M6 stars). Furthermore, disks in this work have been imaged with $\sim 0''.05$

compared to $0''1$ in Long et al. (2019). A complete sample around mid- to late M stars and higher-resolution imaging of the inner regions of disks around solar-like stars are needed to evaluate any difference in their cavity occurrence rate in millimeter wavelength.

Gap+ring pairs are only detected in the large double ring disk 2M0412. 2M0434 has a ring located at about 10 au, while its dust disk size is about 80 au; the very extended emission in between may hold shallow rings and gaps inside. Rings around 2M0436 and 2M0508 have radial widths comparable to the beam size and hence are not resolved—at higher resolution they might be resolved into multiple narrower rings (e.g., Facchini et al. 2020; Pérez et al. 2020). It is also possible that fainter rings at large radii are not recovered with current sensitivity. Observations with a spatial resolution that is smaller than the pressure scale height and with deeper sensitivity are needed to have complete characterization of substructure type and occurrence rate in disks around mid- to late M stars.

Smooth disks 2M0450 and CIDA 12 are candidates to host small cavities (Section 3.2.2). Though their visibility profiles do not show clear null points (Figure 2), small cavities below 5 au could remain hidden at our current angular resolution, especially for CIDA 12, which has an inclination of $\sim 65^\circ$ (see analysis of high-inclination disks by van der Marel et al. 2022).

ALMA revealed a central depression of large grains in four structured disks in our sample. The SED complements ALMA imaging by providing information on small grains, since deficits of near-infrared emission indicate an inner disk clearing of small dust grains. Figure 5 shows the collected photometry and the modeled SEDs with modeling processes given in Appendix D. In short, the modeling uses a continuous disk component with a cavity sized $R_{\mu\text{m},\text{in}}$ and an outer radius adopting $R_{90\%,\text{dust}}$ retrieved from millimeter images (Table 3). The goal is not to have a stringent constraint on disk parameters, since the available infrared photometry is limited, but to have a rough sense of the cavity sizes of small dust grains and how they compare to the millimeter-sized grains observed by ALMA. Since we lack knowledge of other parameters describing disk density profiles (e.g., power-law index of surface density and pressure scale height), the cavity size is degenerated with other parameters, including the power index for dust mass density and the pressure scale height. Through experiments, the constrained cavity sizes of small dust grains can differ by a few astronomical units under different combinations of other parameters. However, the uncertainty on cavity sizes does not affect the discussions below.

For the four disks with cavities in millimeter images, three disks show evidence of inner dust clearing from their SEDs. 2M0412's SED is consistent with $R_{\mu\text{m},\text{in}} \sim 0.9$ au for small dust grains, which is far smaller than its ~ 60 au millimeter cavity. 2M0434 and 2M0508 are consistent with $R_{\mu\text{m},\text{in}} \sim 4$ au cavities. This test of simple SED fitting suggests that micron-sized dust grains are not as depleted as millimeter-sized grains in the cavity, consistent with a morphology that is also seen around larger and more massive disks with both scattered light and ALMA images (Villenave et al. 2019). $R_{\mu\text{m},\text{in}}$ for 2M0436 is around 0.03 au, consistent with dust sublimation radius, so there is no evidence for clearing of small grains. There is evidence of an inner disk around 2M0436 from both its brightness profile (Figure 4) and its visibility fitting result (Section 3.1). Models with the same inclination as that from 2M0436's ALMA image have a bit of difficulty in reproducing

the high flux at near-infrared. These suggest that 2M0436 may host a puffed up or misaligned inner disk (e.g., Dullemond et al. 2001; van der Marel et al. 2018, 2022). For the two smooth disks, 2M0450 shows no clear small grain cavity with $R_{\mu\text{m},\text{in}}$ consistent with dust sublimation radius, while CIDA 12 shows evidence of a 0.3 au cavity. Further evaluation of these potential cavities will require follow-up at much higher spatial resolution and sensitivity. Scattered light imaging would likely require the next generation of ground-based telescopes, since these disks are too faint to observe with current ground-based telescopes and the cavities are too small for JWST imaging.

4.3. Origins of Small Cavities

Rings are the most common substructures in our sample, similar to surveys on disks around early-type stars such as DSHARP (Andrews et al. 2018a; Huang et al. 2018a) and the Taurus survey (Long et al. 2018). With the current resolution and sensitivity of our observations, the detected rings all appear axisymmetric, without significant azimuthally asymmetric features. Most rings encircle cavities, except for the outer ring of 2M0412 (see Long et al. 2023 for a detailed analysis of the origins of substructures of the 2M0412 disk). In short, planet-disk interaction is preferred over other mechanisms in 2M0412, with Saturn-mass planets capable of shaping the observed disk morphology. However, a combination of dead zones and photoevaporation cannot be ruled out. Below we focus on discussion of possible origins²¹ for substructures of 2M0434, 2M0436, and 2M0508, which show small cavities around 10 au.

Condensation Fronts. Major volatiles in protoplanetary disks freeze onto dust grains from the gas phase as the disk temperature decreases outward. Across these regions, which are referred to as condensation fronts or ice lines, the dust opacity and critical fragmentation velocity are expected to change and further ring/gap substructures can be produced (e.g., Zhang et al. 2015; Okuzumi et al. 2016).

We consider an irradiated flared disk with a disk midplane temperature formulated as Equation (6), where the flaring angle ϕ_{fl} is assumed to be 0.02 (e.g., Dullemond et al. 2018; Huang et al. 2018a). The ice-line location of a volatile can be calculated from a stellar luminosity and the freezing point of the molecule. Since ice lines of abundant species like H_2O and NH_3 are close to the host star (< 2 au) and are not resolvable by our observations, we focus on species with lower condensation temperatures in Zhang et al. (2015), which are clathrate-hydrated CO and N_2 (41–46 K), CO (23–28 K), and N_2 (12–15 K).

The comparison between ice-line locations and brightness profiles from best-fit models is shown in Figure 6. Interestingly, the peak emission radii are all close to the CO ice lines. However, inferring the ice-line radius is a challenging task. Besides the uncertainties in the estimation of disk midplane temperature (e.g., Liu 2021), ice lines can be thermally unstable and dynamically evolve on timescales from 1000 to 10,000 yr (Owen 2020). In simulations, ice lines have not been found to carve out cavities (see Pinilla et al. 2017b for a simulation

²¹ We exclude the dead zone outer edge as a possible origin of radial dust traps. In the up-to-date picture where all three nonideal MHD effects are considered, the level of MRI turbulence is damped smoothly in the outer disk (no abrupt change). As a result, a dead zone outer edge will not develop (see, e.g., Figure 2 in Bai 2016).

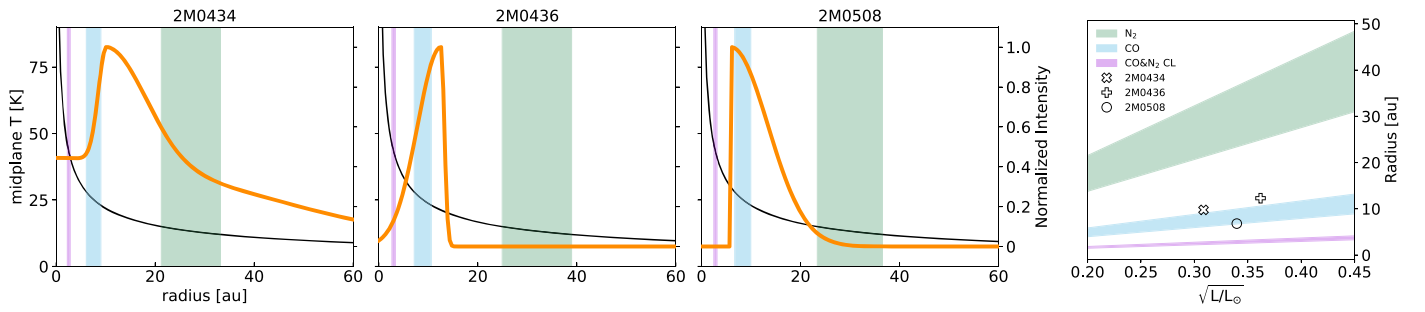


Figure 6. Left three panels: disk midplane temperature profiles calculated using Equation (6) are shown as black curves. Orange curves show the normalized radial profile of best-fit models from visibility fitting. Shaded regions are the ice-line locations for N_2 (light green), CO (light blue), and clathrate-hydrated CO and N_2 (light purple). Right panel: disk radius vs. the square root of stellar luminosity. The peak model intensity locations are shown for 2M0434 (cross), 2M0436 (plus sign), and 2M0508 (circle). The shaded regions for ice lines are the same as in the left panels.

around a Herbig AeBe star). Deeper observations of CO isotopologues are needed to better constrain disk midplane temperature, and future simulations tailored to M stars could together help determine the contribution of ice lines to the cavities/rings detected.

Photoevaporation and MHD Wind. When the mass-loss rate by photoevaporation surpasses the accretion rate through the disk, a gas and dust gap will open in the disk. Recent photoevaporation models by Picogna et al. (2019) predict transition disks with accretion rates $\leq 10^{-9} M_{\odot} \text{ yr}^{-1}$ and maximum cavity sizes of about 30 au when surrounding solar-type stars. The lower mass-loss rate at large radii around very low mass stars (Picogna et al. 2021) will likely lead to a smaller maximum cavity size, which we expect to be above 10 au. This is because the old photoevaporation models around $0.1 M_{\odot}$ stars by Owen et al. (2012) have cavities ≤ 10 au and new mass-loss profiles by Picogna et al. (2019) are more efficient at removing material at larger disk radii, which will lead to larger cavities. We therefore expect that the maximum cavity size around very low mass stars will fall between 10 and 30 au. 2M0434’s 10 au cavity, 2M0436’s 12 au cavity, and their accretion rates of about a few $\times 10^{-10} M_{\odot} \text{ yr}^{-1}$ fall in the predicted parameter space.

Further evaluating the role of photoevaporation in the creation of cavities will require additional observations. Possible discriminators include high angular resolution imaging of the gas—in this paper, we have limited sensitivity that allows us to only tentatively identify a cavity around one source, 2M0508. In addition, empirical measurements of photoevaporation rates through lines of O I and Ne II (Pascucci et al. 2011) but the results are challenging to interpret (e.g., Banzatti et al. 2019; Fang et al. 2023b; Rab et al. 2023), given the possibility that these lines may form in a magnetothermal wind (e.g., Wang et al. 2019).

Furthermore, accreting transition disks could be sustained by other mechanisms. Gárate et al. (2021) showed that a disk with X-ray photoevaporation in combination with dead zones can reproduce both the accretion rates and gap sizes observed in transition disks. Their models predict a long-lived compact inner disk, which is not seen in our ALMA images under current resolution and sensitivity. MHD wind as another scenario, if the large-scale magnetic field distribution is not significantly modified, could generate a positive radial slope of the gas surface density (e.g., Suzuki et al. 2016), which inhibits the inward drift of pebbles, and sustain accretion rates similar to those of classical T Tauri stars (e.g., Lesur 2021; Martel & Lesur 2022).

Embedded Planets. Giant planets can open gaps in the gas disks and form gas pressure bumps that trap dust particles outside its orbit. Dust cavities will then form after the inner dust disk materials are accreted onto the star. By applying the analytical criterion for opening a gap in the gas (Crida et al. 2006), the estimated masses of planets needed to open the small cavities in our disk sample are as follows: for viscous $\alpha \sim 10^{-4}$ and 10^{-3} , $0.1 M_{\text{Jup}}$ and $0.3 M_{\text{Jup}}$ at ~ 8 au for 2M0434, $0.1 M_{\text{Jup}}$ and $0.3 M_{\text{Jup}}$ at ~ 10 au for 2M0436, and $0.1 M_{\text{Jup}}$ and $0.2 M_{\text{Jup}}$ at ~ 6 au for 2M0508. The locations of planets are assumed to be five times the Hill radius $r_H = r_p (M_p/3M_*)^{1/3}$ away from the ring peak locations (e.g., Dodson-Robinson & Salyk 2011). Since only 2M0508 shows a tentative gas cavity, these planet masses should be treated as upper limits. Moreover, if the disk mass and angular momentum transport are dominated by MHD wind rather than turbulent viscosity, planets can open wider and deeper gaps more easily (e.g., Elbakyan et al. 2022; Aoyama & Bai 2023; Wafflard-Fernandez & Lesur 2023). As a result, the masses of embedded planets could be a factor of a few to 10 smaller than estimated above (Elbakyan et al. 2022).

Simulations of planet–disk interaction predict the segregation between millimeter-sized dust continuum emission peak and gas emission peak (or micron-sized dust; e.g., de Juan Ovelar et al. 2013; Facchini et al. 2018). We find hints of such segregation between micron-sized and millimeter-sized dust grains from SEDs (Section 4.2). For gas emission, only 2M0508 shows tentative inner gas depletion, and the gas peak location overlaps with the ring location. Deeper sensitivity and higher angular resolution of molecular line mapping are needed to resolve the gas depletion in the inner disk if present.

Taking disk dust masses in Section 3.4 and assuming a gas-to-dust mass ratio of 100, the estimated current disk masses are $6.1 M_{\text{Jup}}$ for 2M0434, $0.5 M_{\text{Jup}}$ for 2M0436, and $0.8 M_{\text{Jup}}$ for 2M0508. If we assume a constant accretion rate after disk formation, then the total mass accreted onto the star from the disk is $1.5 M_{\text{Jup}}$ for 2M0434 and $4.5 M_{\text{Jup}}$ for 2M0436 (using stellar ages with 50% spot coverage). The planet masses needed to open cavities for 2M0434 and 2M0436 are within 10% of their estimated total disk masses at initial stages. If 2M0508 has an accretion rate $\sim 3 \times 10^{-10} M_{\odot} \text{ yr}^{-1}$, similar to those in our sample (Table 1), and that accretion rate has remained constant (most likely, the accretion rate at earlier stages of formation was higher; e.g., Fischer et al. 2017; Fang et al. 2023a), its potential planet mass is also within 10% of disk mass. Hence, from the perspective of disk mass budget, the three small cavity disks had enough materials to form those Saturn-mass planets (e.g., Boss 2006; Lin et al. 2018).

If the observed cavities are carved out by giant planets, how does the current detection rate of cavities around mid- to late M stars compare to the occurrence rate of exoplanets? The detection rate of cavities around mid- to late M stars in Taurus is around 24%, given the fraction of 7/13 for cavities in disks (Section 4.2) and accounting for the disk fraction around 45% for M3–M6 stars in Taurus (Esplin & Luhman 2019; the latter correction applies only if the age spread of the sample is much less than the disk survival timescale). However, this is likely higher than the real cavity rate, since the sample of 13 disks is slightly biased to the brighter end of disks around M3–M6 stars. As for exoplanets around M dwarfs, the CARMENES survey obtained occurrence rates for giant planets with $M_p \sin i > 100 M_\oplus$ and periods of 1–1000 days of $0.021^{+0.018}_{-0.011}$ planets per star and $0.045^{+0.021}_{-0.016}$ planets per star for stars less and more massive than $0.337 M_\odot$, respectively (Ribas et al. 2023). Wide-orbit (>10 au) giant planets more massive than Jupiter are found to be rare around M dwarfs (e.g., Bowler et al. 2015). Currently, the constraints on sub-Jovian giants on orbits of a few astronomical units around M dwarfs are limited. Measurements around Sun-like stars show that giant planet occurrence is enhanced by a factor of four beyond 1 au compared to within 1 au (e.g., Fernandes et al. 2019; Fulton et al. 2021), while it is unclear whether the result could be extrapolated to M dwarfs. Samples from both disks and exoplanets need to be developed to make a robust comparison.

Binary Companions. Binary stars could also carve out inner cavities in circumbinary disks, with the cavity sizes expected to be 3–5 times the binary semimajor axis (e.g., Artymowicz & Lubow 1994; Miranda et al. 2017). Hence, stellar companions within 4 au could be responsible for the 7–12 au cavities in the three disks. To our knowledge, no evidence of stellar multiplicity has been found in our sample (Kraus et al. 2011; Kraus & Hillenbrand 2012), although the scales of a few au have yet to be explored. If the companions are sufficiently massive (mass ratios > 0.1 – 0.2), the binary would produce eccentric cavities (0.05–0.35 for circular binaries; Miranda et al. 2017; Ragusa et al. 2020) and cause a shift between the stellar mass center and the geometric center of the cavity. For the ~ 10 au cavities in our sample, resolutions better than the binary separation are needed to detect the potential shift.

Among the mechanisms described above, photoevaporation and planets are more preferred origins of small cavities (around 7 and 10 au) in our sample. To distinguish between these possibilities, more deep and higher angular resolution observations of molecular lines are needed. Furthermore, multi-wavelength analysis of the spectral index at the cavity edge might help to distinguish photoevaporation and planet scenarios (Picogna et al. 2023), where a cavity created by photoevaporation is expected to have a higher spectral index owing to its lower dust filtering efficiency.

5. Summary

This paper presents high angular resolution (~ 50 mas, 8 au) ALMA Band 6 observations of six disks around mid- to late M stars in Taurus. We characterize the disk continuum emission by fitting parametric models in the visibility plane. We explore these disks’ global properties and the possible origins of their substructures. The main findings are summarized as follows:

1. We detect all six disks in millimeter continuum emission. ^{12}CO is detected in five disks with a marginal detection in

2M0450, and ^{13}CO is detected in 2M0412 and 2M0434. Dust substructures are detected in four disks: 2M0412, 2M0434, 2M0436, and 2M0508, which are also the four brightest disks in our sample. We perform fitting in the visibility plane, with rings modeled as radially asymmetric Gaussian rings. With our current sensitivity (~ 40 mJy beam $^{-1}$) and spatial resolution, 2M0412 show a large cavity surrounded by a ring at 60 au, followed by a gap and an outer dust ring at 110 au; the other three disks all display a cavity surrounded by a dust ring at 10 au for 2M0434, 12 au for 2M0436, and 7 au for 2M0508.

2. The Nuker profile fitting on the two compact smooth disks 2M0450 and CIDA 12 shows that they may hold small cavities, with sizes being ~ 1.7 au for 2M0450 and ~ 5.7 au for CIDA 12. Current spatial resolution and sensitivity may hide these small and shallow cavities. Nuker profiles can reproduce the flux for CIDA 12 better than a Gaussian profile, with the flux from the Nuker profile being twice as much as Gaussian’s flux. Higher spatial resolution is needed to resolve the potential cavities.
3. The structured disks are brighter than the smooth disks in our sample; the presence of dust trapping by substructures could account for this. 2M0436 and 2M0508 deviate from the flatter $L_{\text{mm}}-M_*$ relation for structured disks, which could be due to a combination of partially optical thickness and boulder formation (Pinilla et al. 2018, 2020). Disks around 2M0436, 2M0450, CIDA 12, and 2M0508 fall at the faint end of the $L_{\text{mm}} \propto R_{\text{eff}}^2$ relation, consistent with being radial drift dominated. After measuring the ratios between gas disk size $R_{\text{gas},90\%}$ and the dust disk size $R_{\text{dust},90\%}$, 2M0436 and 2M0450 show large ratios $R_{\text{gas},90\%}/R_{\text{dust},90\%} \sim 5$, indicating very efficient dust radial drift in these two disks.
4. All structured disks in our sample show a central cavity, indicating the clearing of millimeter-sized dust grains. Radiative transfer fits to SEDs to provide a rough constraint on the clearing of micron-sized dust particles. Of the four structured disks, only 2M0436 does not show evidence of clearing of micron dust, with the modeled cavity size being the dust sublimation radius. 2M0412 shows a 0.9 au cavity size far smaller than its millimeter cavity. 2M0434 and 2M0508 show 4 au cavities for micron dust. For the two smooth disks, CIDA 12 shows a 0.3 au cavity consistent with its near-IR deficit. These SED-derived cavity sizes are smaller than their counterpart in millimeter images.
5. Various mechanisms could be responsible for the observed substructures. For 2M0412, Long et al. (2023) show that Saturn-mass planets are able to carve out its cavity and gap. The large cavity alone can also be shaped by a combination of dead zone and photoevaporation. 2M0412’s large rings are unlikely to be related to ice lines. For the other three disks, Saturn-mass planets or photoevaporation could be responsible for their cavities around 10 au. Ice lines could also play a role, but their locations are highly uncertain. High-resolution mapping of gas emission and multiwavelength analysis of the spectral index at the edge of cavities could help to distinguish different mechanisms.

Our sample covers a wide range of millimeter luminosity; the four cavity disks together with the other two harboring potential small cavities suggest that substructures are likely ubiquitous in disks around mid- to late M stars. Current exoplanet statistics does not rule out that all these observed cavities are created by giant planets.

High spatial resolution imaging of disks around mid- to late M stars is still very limited in number. The more frequent small cavities of around 10 au around those disks may originate from various mechanisms, which will make them great laboratories for testing planet formation and disk physics.

Acknowledgments

G.J.H. and Y.S. are supported by the National Key R&D Program of China No. 2019YFA0405100 and by grant 12173003 from the National Natural Science Foundation of China. Support for F.L. was provided by NASA through the NASA Hubble Fellowship grant No. HST-HF2-51512.001-A awarded by the Space Telescope Science Institute, which is operated by the Association of Universities for Research in Astronomy, Incorporated, under NASA contract NAS5-26555. D.H. is supported by a Center for Informatics and Computation in Astronomy (CICA) grant and grant No. 110J035319 from the Ministry of Education of Taiwan. D.H. also acknowledges support from the National Science and Technology Council of Taiwan through grant No. 111B3005191. P.P. acknowledges support from the UK Research and Innovation (UKRI) under the UK government’s Horizon Europe funding guarantee from ERC (under grant agreement No. 101076489). E.R. acknowledges financial support from the European Union’s Horizon Europe research and innovation program under the Marie Skłodowska-Curie grant agreement No. 101102964 (ORBIT-D). E.R. also acknowledges financial support from the European Research Council (ERC) under the European Union’s Horizon 2020 research and innovation program (grant

agreement No. 864965, PODCAST). D.J. is supported by NRC Canada and by an NSERC Discovery Grant. C.F.M. is funded by the European Union (ERC, WANDA, 101039452). Views and opinions expressed are, however, those of the author(s) only and do not necessarily reflect those of the European Union or the European Research Council Executive Agency. Neither the European Union nor the granting authority can be held responsible for them. G.D.M. acknowledges support from FONDECYT project 11221206, from ANID—Millennium Science Initiative—ICN12_009, and from the ANID BASAL project FB210003. L.A.C. acknowledges support from FONDECYT project 1211656 from ANID and the Millennium Science Initiative, Center Code NCN2021_080.

This paper makes use of the following ALMA data: ADS/JAO.ALMA#2019.1.00566.S. ALMA is a partnership of ESO (representing its member states), NSF (USA) and NINS (Japan), together with NRC (Canada), MOST and ASIAA (Taiwan), and KASI (Republic of Korea), in cooperation with the Republic of Chile. The Joint ALMA Observatory is operated by ESO, AUI/NRAO and NAOJ. The National Radio Astronomy Observatory is a facility of the National Science Foundation operated under cooperative agreement by Associated Universities, Inc.

Facility: ALMA.

Software: CASA (CASA Team et al. 2022), GALARIO (Tazzari et al. 2018), emcee (Foreman-Mackey et al. 2013), RADMC-3D (Dullemond et al. 2012).

Appendix A CO Channel Maps and Moment Maps

Moment maps of ^{12}CO and ^{13}CO (if detected) are shown in Figure A1, and corresponding channel maps are shown in Figures A2–A7.

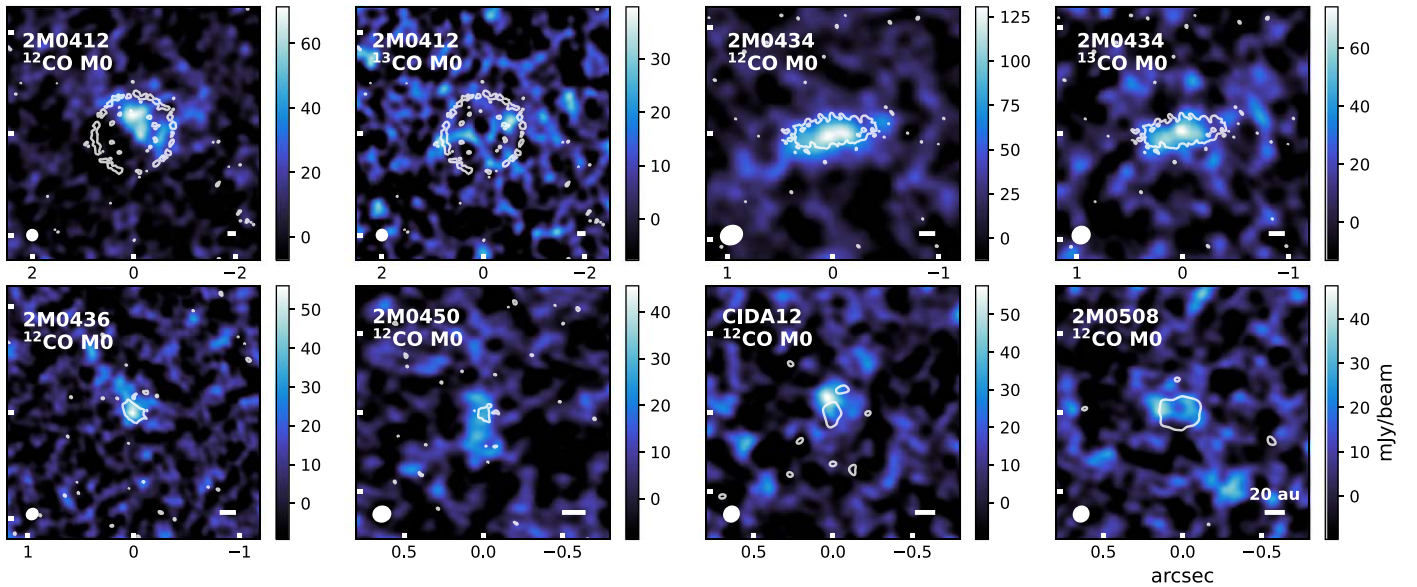


Figure A1. Moment 0 maps for (marginally) detected ^{12}CO and ^{13}CO . The 3σ white contours from dust continuum images are overlaid. For each panel, beams are shown as white ellipses at lower left and 20 au white scale bars are shown at lower right.

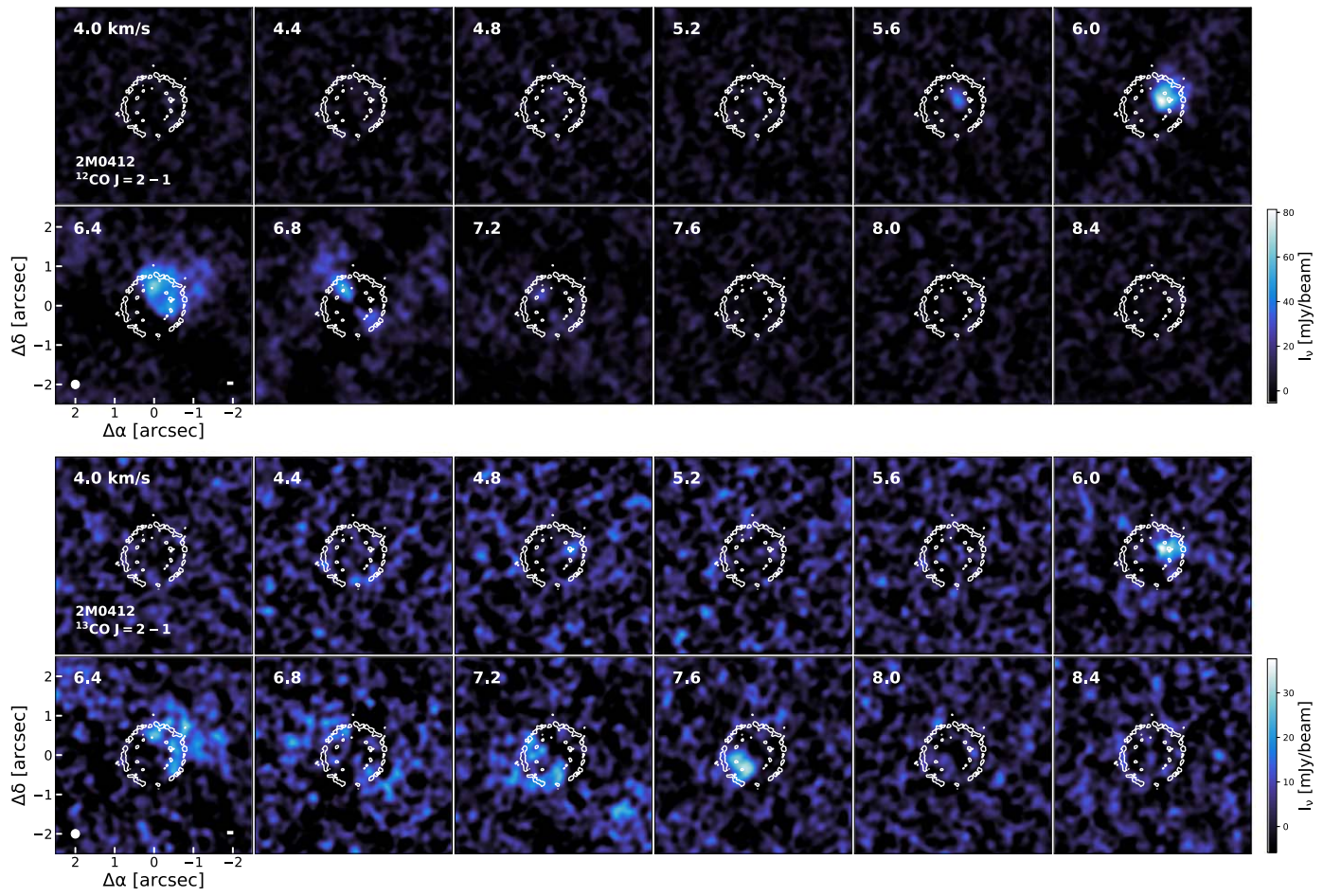


Figure A2. Channel maps of ^{12}CO (top) and ^{13}CO (bottom) for 2M0412. Central velocities are given in the upper left corner of each channel in units of km s^{-1} . The 3σ white contours from dust continuum images are overlaid. Beams as white ellipses and 20 au white scale bars are shown at lower left and lower right, respectively.

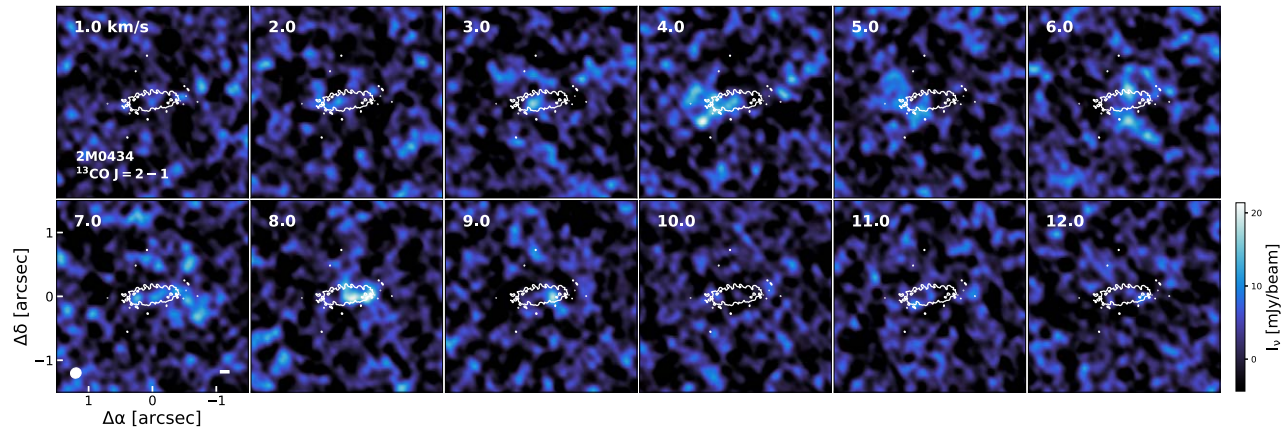
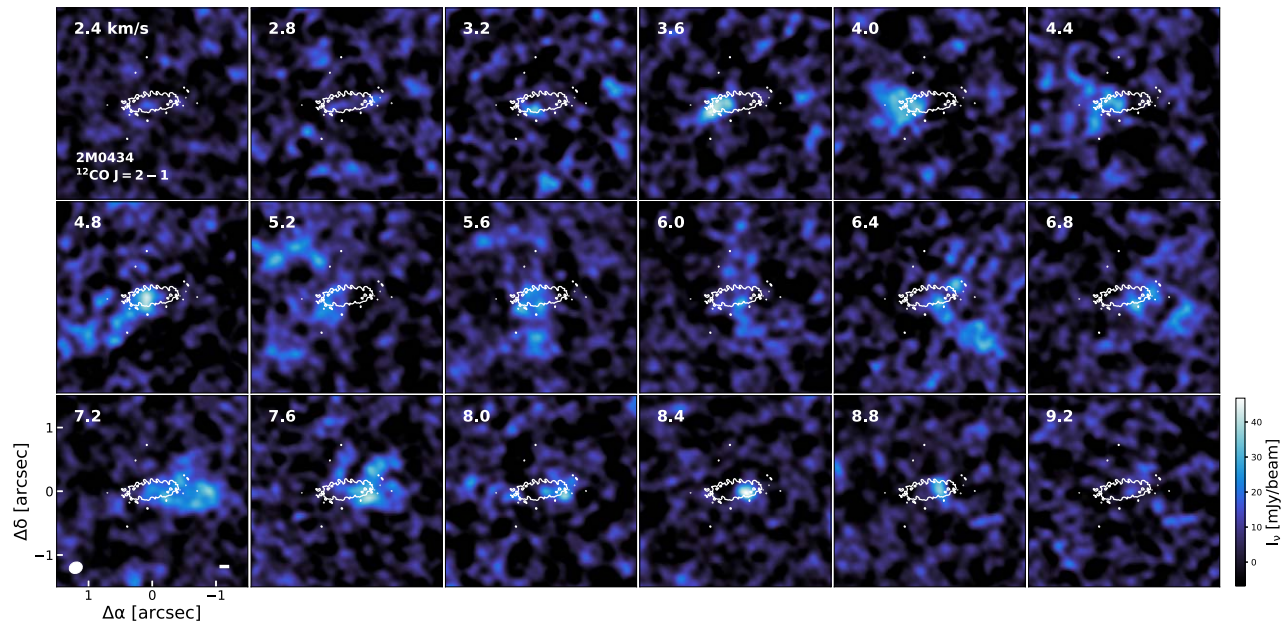


Figure A3. Same as Figure A2, but for 2M0434.

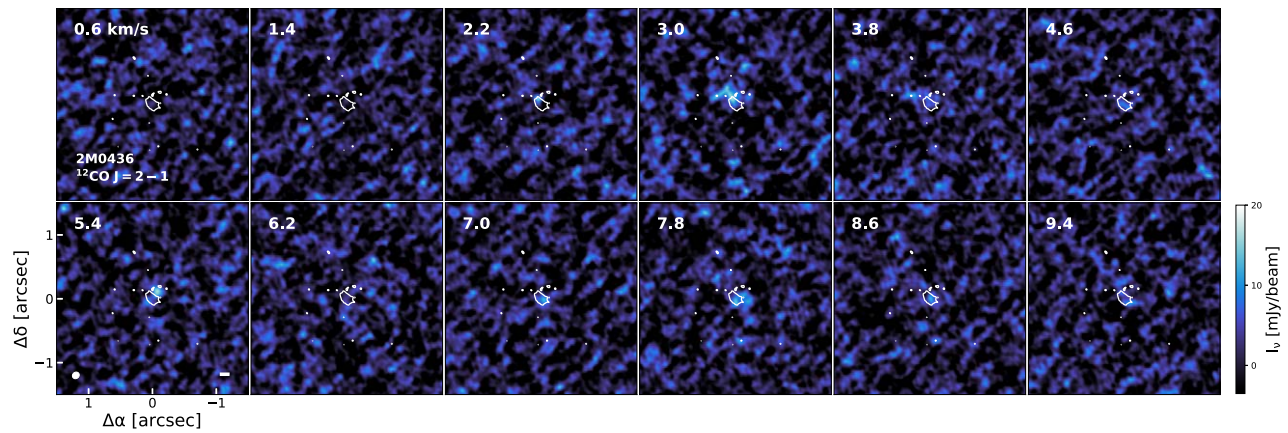


Figure A4. Same as Figure A2, but for 2M0436.

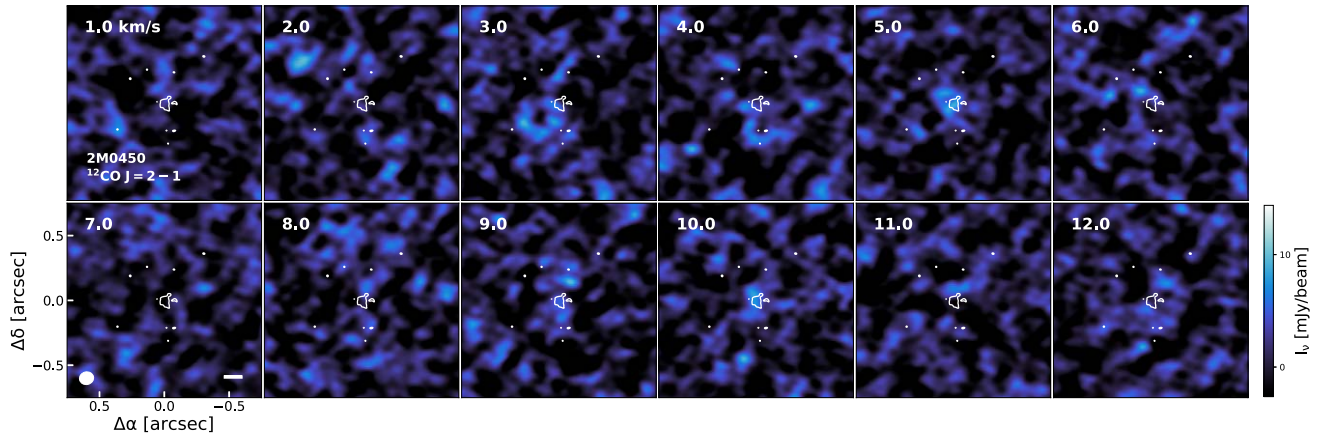


Figure A5. Same as Figure A2, but for 2M0450.

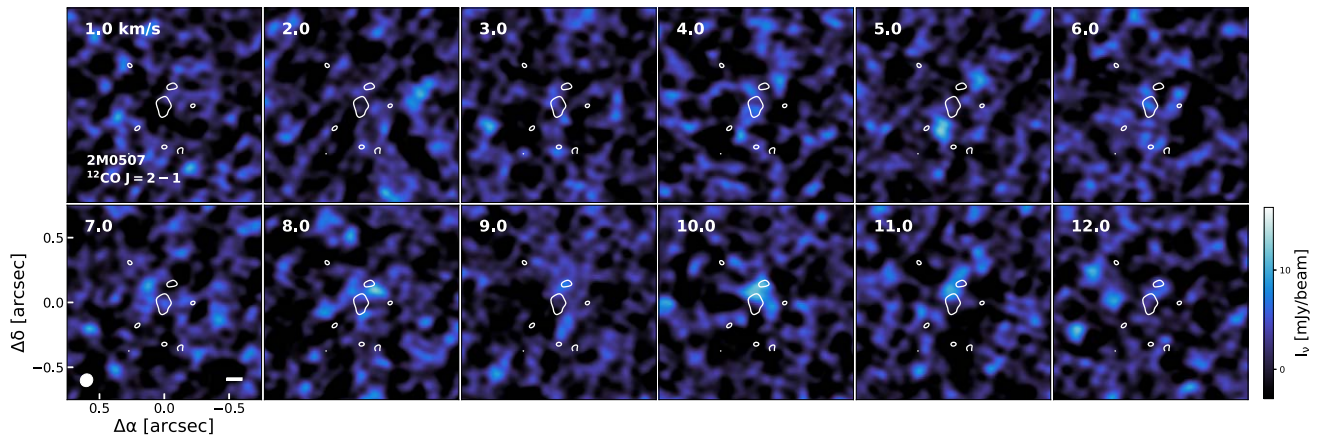


Figure A6. Same as Figure A2, but for CIDA 12.

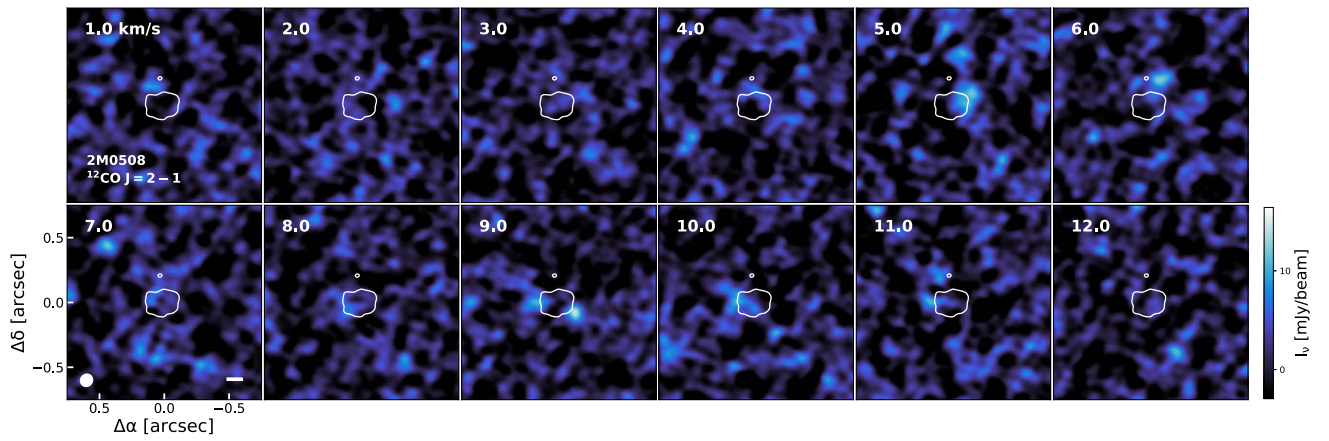


Figure A7. Same as Figure A2, but for 2M0508.

Appendix B

Central Emission in 2M0436?

In this appendix, we test whether 2M0436 has unresolved central emission (Section 3.1). A central point emission is added to the model of a radially asymmetric Gaussian ring, with point-source intensity formulated as $F_1\delta(r)$. F_1 is set to be distributed uniformly between 0 and 1 mJy. Figure B1 shows the best-fit model images and intensity profiles for the two

models. The central point emission model reaches a convergence with the point flux of $0.04^{+0.03}_{-0.03}$ mJy (Figure B2), indicating a nondetection (detection at 1σ) of central emission. Section 3.1 mentioned that it could be that the unresolved central emission blends with the outer ring emission, resulting in a ring with its inner width wider than its outer width, which is contrary to dust trapping in pressure bumps. However, in our attempts to add a central emission component, the outer ring

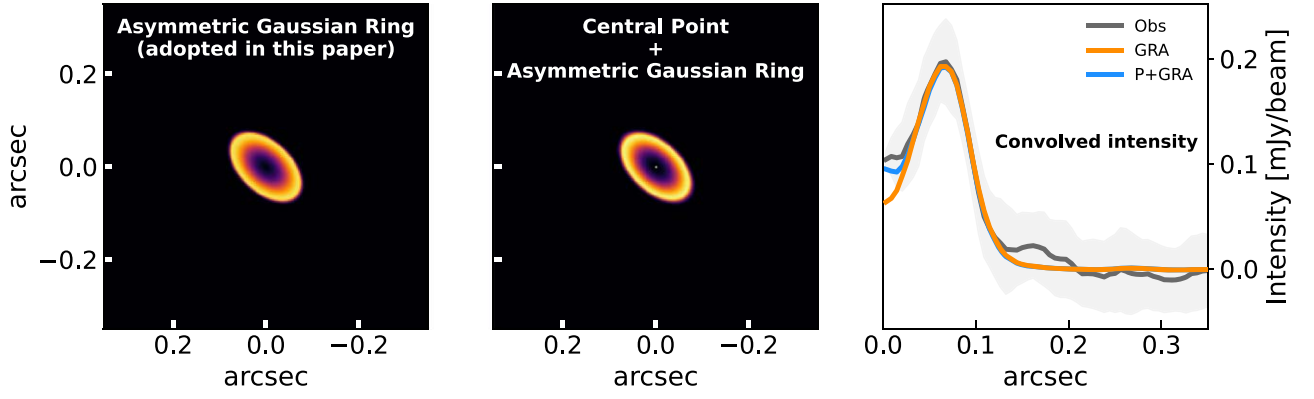


Figure B1. Two different models for 2M0436. From left to right: (1) best-fit image from the model with only an asymmetric Gaussian ring; (2) best-fit image from the model with a central point and an asymmetric Gaussian ring; (3) azimuthally averaged radial profiles retrieved from beam-convolved images.

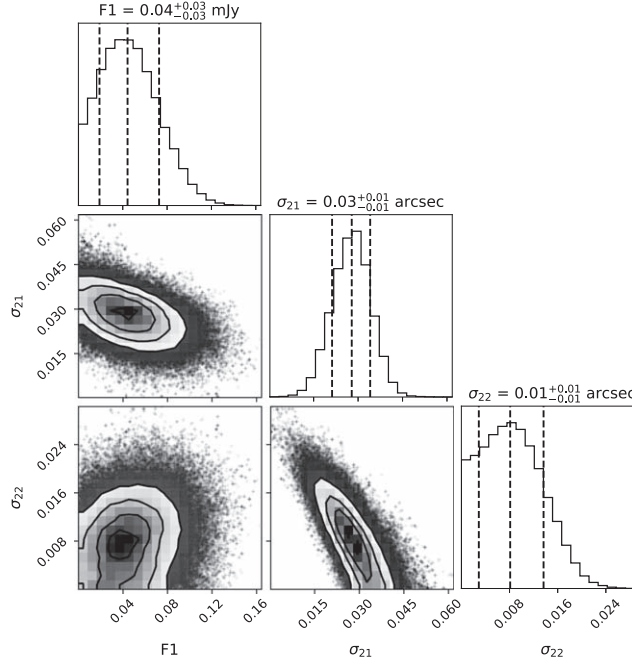


Figure B2. Cornerplots of key parameters of the model, including a central point and an asymmetric Gaussian ring. From left to right, the three parameters are the flux of point emission, the inner width of the ring, and the outer width of the ring.

still shows wider inner width and the ratio between the two widths is similar to that from the ring-only model (Section 3.2.1).

Appendix C

Nuker Fitting Results on 2M0450 and CIDA 12

The modeling procedure follows Section 3.1, with Nuker parameters' priors following Tripathi et al. (2017):

$p(\log_{10} \alpha) = \mathcal{U}(0, 2)$, $p(\beta) = \mathcal{U}(0, 10)$, and γ being sampled approximately uniform over $(-3, 2)$:

$$p(\gamma) \propto \frac{1}{1 + e^{-5(\gamma+3)}} - \frac{1}{1 + e^{-15(\gamma-2)}}. \quad (\text{C1})$$

Figure C1 shows the best-fit Nuker model images, visibilities, and random radial profiles retrieved from posterior distributions.

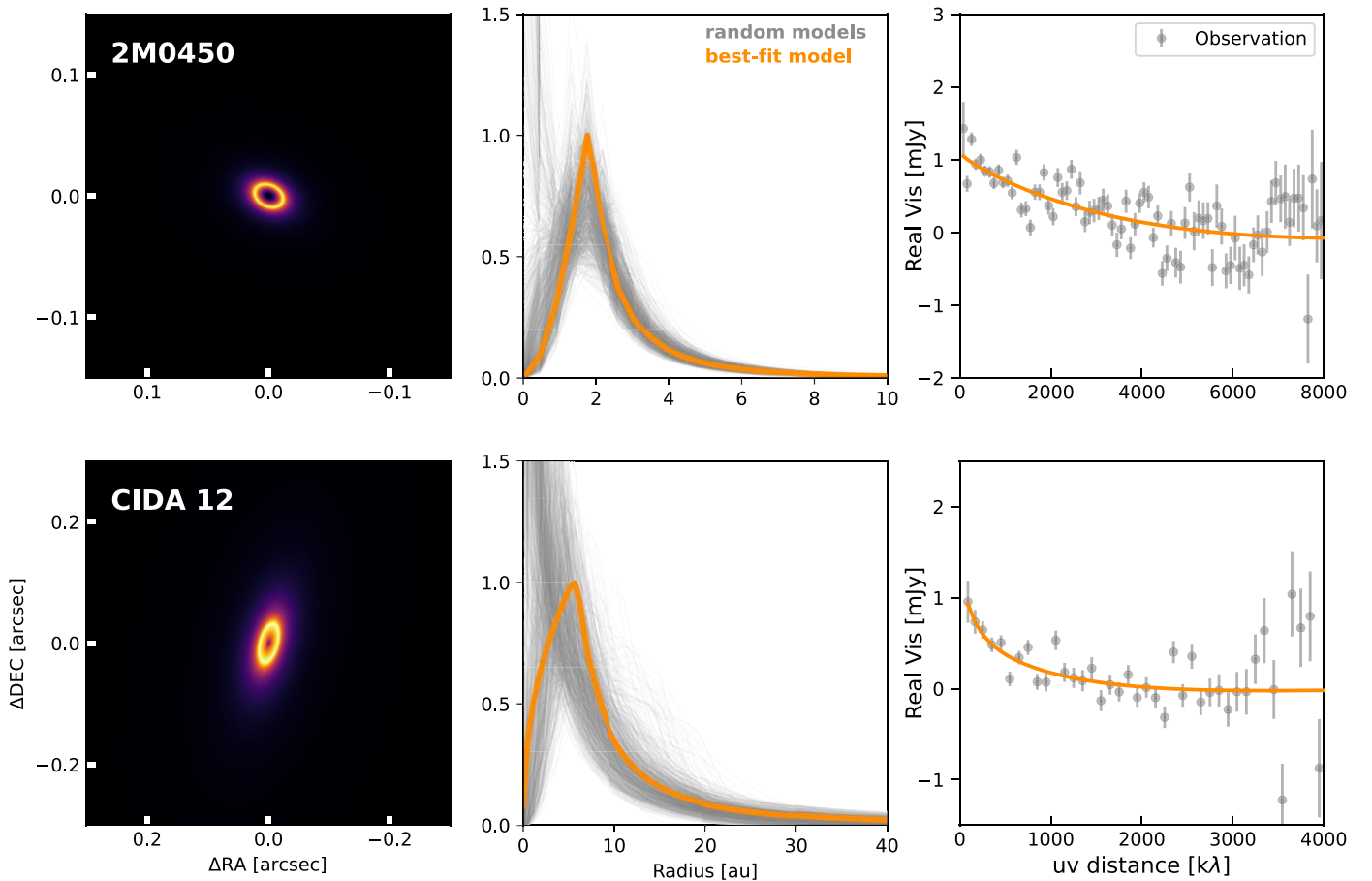


Figure C1. Nuker fitting results of disks that seem to lack structures in the image plane. Columns from left to right: (1) unconvolved best-fit Nuker model images; (2) radial profiles retrieved from best-fit (orange) and 1000 randomly selected (gray) Nuker models; (3) real part of deprojected and binned visibilities from observations and best-fit models.

Appendix D SED Fitting

The SED data points are collected from GALEX GR6+7 (Bianchi et al. 2017), Sloan Digital Sky Survey DR17 (Abdurro’uf et al. 2022), Pan-STARRS (Flewelling et al. 2020), Gaia DR3 (Gaia Collaboration et al. 2023), 2MASS (Skrutskie et al. 2006), WISE (Wright et al. 2010), Spitzer (Luhman et al. 2010), Herschel (Marton et al. 2017), and our measurements at 1.3 mm (literature value at 1.3 mm for CIDA 12 in Akeson et al. 2019).

We fit the photospheric emission of each host star using the BT-Settl models (Allard et al. 2011), with the temperature and extinction in Table 1 and assuming a gravity of $\log g = 4.0$. With the fitted spectrum and stellar luminosity as inputs, we then use the RADMC-3D code (Dullemond et al. 2012) to perform self-consistent radiative transfer to obtain dust temperature profiles and then simulate the SEDs. For a flared disk model with well-mixed dust and gas (for small grains this is approximately correct), the disk mass density profile is given as

$$\rho(r, z) = \frac{\Sigma(r)}{\sqrt{2\pi}H_p} \exp\left(-\frac{z^2}{2H_p^2}\right), \quad (\text{D1})$$

where r is the distance to the central star measured in the disk midplane, z is the distance to the disk midplane, H_p is the

pressure scale height, and Σ is the surface density integrated over the vertical direction. We adopt a simple power law for Σ and H_p :

$$\Sigma(r) = \Sigma_0 \left(\frac{r}{r_{\text{out}}}\right)^p \quad (\text{D2})$$

$$H_p(r) = H_{100} \left(\frac{r}{100 \text{ au}}\right)^\beta, \quad (\text{D3})$$

where H_{100} is the scale height of small dust grains at 100 au and p, β are the slope.

Six parameters are needed to describe the simple flared disk model: $R_{\text{in}}, R_{\text{out}}, p, \beta, H_{100}$, and M_{dust} . We fix p to -1 and R_{out} to the $R_{90\%}$ in millimeter images (Section 3.4 and Table 3). M_{dust} is first set to the estimated value in Table 3 and adjusted to match the $F_{1.3 \text{ mm}}$. We note that M_{dust} has a negligible effect on the infrared SEDs (and hence the parameter R_{in}) since dust is optically thick at that wavelength. We test each combination of the other three parameters with R_{in} between dust sublimation radius and millimeter cavity size, β in $[1.0, 1.2]$ and H_{100} in $[5, 15]$. As for the dust prescription, we adopt the model in Birnstiel et al. (2018) with grain sizes ranging from 0.01 to 1000 μm . The parameters of our best-fit models are listed in Table D1, and Figure 5 shows the comparison between the models and observations.

Table D1
Best-fit Models for SED

Parameters	2M0412	2M0434	2M0436	2M0450	CIDA 12	2M0508	Unit
R_{in}	0.90	4	0.03	0.02	0.3	4	au
R_{out}	126	82	14	6	20	21	au
p	-1	-1	-1	-1	-1	-1	...
β	1.15	1.20	1.15	1.15	1.20	1.15	...
H_{100}	10.0	7.5	12.5	10.0	6.3	7.5	au

ORCID iDs

Yangfan Shi (施杨帆)  <https://orcid.org/0000-0001-9277-6495>
 Feng Long (龙凤)  <https://orcid.org/0000-0002-7607-719X>
 Gregory J. Herczeg (沈雷歌)  <https://orcid.org/0000-0002-7154-6065>
 Daniel Harsono  <https://orcid.org/0000-0001-6307-4195>
 Yao Liu  <https://orcid.org/0000-0002-7616-666X>
 Paola Pinilla  <https://orcid.org/0000-0001-8764-1780>
 Enrico Ragusa  <https://orcid.org/0000-0001-5378-7749>
 Doug Johnstone  <https://orcid.org/0000-0002-6773-459X>
 Xue-Ning Bai  <https://orcid.org/0000-0001-6906-9549>
 Ilaria Pascucci  <https://orcid.org/0000-0001-7962-1683>
 Carlo F. Manara  <https://orcid.org/0000-0003-3562-262X>
 Gijs D. Mulders  <https://orcid.org/0000-0002-1078-9493>
 Lucas A. Cieza  <https://orcid.org/0000-0002-2828-1153>

References

- Abdurro'uf, Accetta, K., Aerts, C., et al. 2022, *ApJS*, 259, 35
 Akeson, R. L., Jensen, E. L. N., Carpenter, J., et al. 2019, *ApJ*, 872, 158
 Allard, F., Homeier, D., & Freytag, B. 2011, in ASP Conf. Ser. 448, 16th Cambridge Workshop on Cool Stars, Stellar Systems, and the Sun, ed. C. Johns-Krull, M. K. Browning, & A. A. West (San Francisco, CA: ASP), 91
 ALMA Partnership, Brogan, C. L., Pérez, L. M., et al. 2015, *ApJL*, 808, L3
 Andrews, S. M. 2020, *ARA&A*, 58, 483
 Andrews, S. M., Huang, J., Pérez, L. M., et al. 2018a, *ApJL*, 869, L41
 Andrews, S. M., Rosenfeld, K. A., Kraus, A. L., & Wilner, D. J. 2013, *ApJ*, 771, 129
 Andrews, S. M., Terrell, M., Tripathi, A., et al. 2018b, *ApJ*, 865, 157
 Ansdell, M., Williams, J. P., Manara, C. F., et al. 2017, *AJ*, 153, 240
 Ansdell, M., Williams, J. P., Trapman, L., et al. 2018, *ApJ*, 859, 21
 Ansdell, M., Williams, J. P., van der Marel, N., et al. 2016, *ApJ*, 828, 46
 Aoyama, Y., & Bai, X.-N. 2023, *ApJ*, 946, 5
 Artymowicz, P., & Lubow, S. H. 1994, *ApJ*, 421, 651
 Bae, J., Isella, A., Zhu, Z., et al. 2023, in ASP Conf. Ser. 534, Protostars and Planets VII, ed. S. Inutsuka et al. (San Francisco, CA: ASP), 423
 Bai, X.-N. 2016, *ApJ*, 821, 80
 Banzatti, A., Pascucci, I., Edwards, S., et al. 2019, *ApJ*, 870, 76
 Barenfeld, S. A., Carpenter, J. M., Ricci, L., & Isella, A. 2016, *ApJ*, 827, 142
 Barenfeld, S. A., Carpenter, J. M., Sargent, A. I., Isella, A., & Ricci, L. 2017, *ApJ*, 851, 85
 Bianchi, L., Shiao, B., & Thilker, D. 2017, *ApJS*, 230, 24
 Birnstiel, T., Dullemond, C. P., Zhu, Z., et al. 2018, *ApJL*, 869, L45
 Boss, A. P. 1997, *Sci*, 276, 1836
 Boss, A. P. 2006, *ApJ*, 643, 501
 Boss, A. P., & Kanodia, S. 2023, *ApJ*, 956, 4
 Bowler, B. P., Liu, M. C., Shkolnik, E. L., & Tamura, M. 2015, *ApJS*, 216, 7
 Bryant, E. M., Bayliss, D., & Van Eylen, V. 2023, *MNRAS*, 521, 3663
 Burn, R., Schlecker, M., Mordasini, C., et al. 2021, *A&A*, 656, A72
 CASA Team, Bean, B., Bhatnagar, S., et al. 2022, *PASP*, 134, 114501
 Cieza, L. A., González-Ruilova, C., Hales, A. S., et al. 2021, *MNRAS*, 501, 2934
 Cieza, L. A., Ruíz-Rodríguez, D., Hales, A., et al. 2019, *MNRAS*, 482, 698
 Crida, A., Morbidelli, A., & Masset, F. 2006, *Icar*, 181, 587
 Curone, P., Izquierdo, A. F., Testi, L., et al. 2022, *A&A*, 665, A25
 Cutri, R. M., Skrutskie, M. F., van Dyk, S., et al. 2003, *yCat*, II/246
 Daemgen, S., Bonavita, M., Jayawardhana, R., Lafrenière, D., & Janson, M. 2015, *ApJ*, 799, 155
 de Juan Ovelar, M., Min, M., Dominik, C., et al. 2013, *A&A*, 560, A111
 Diaz Trigo, M., Carpenter, J., Maude, L., Miura, R., & Plunkett, A. 2019, ALMA Cycle 7 Proposer's Guide, Zenodo, doi:10.5281/zenodo.4511962
 Dodson-Robinson, S. E., & Salyk, C. 2011, *ApJ*, 738, 131
 Dong, R., Liu, S.-y., Eisner, J., et al. 2018, *ApJ*, 860, 124
 Dullemond, C. P., Birnstiel, T., Huang, J., et al. 2018, *ApJL*, 869, L46
 Dullemond, C. P., Dominik, C., & Natta, A. 2001, *ApJ*, 560, 957
 Dullemond, C. P., Juhasz, A., Pohl, A., et al. 2012, RADMC-3D: A Multi-purpose Radiative Transfer Tool, Astrophysics Source Code Library, ascl:1202.015
 Elbakyan, V., Wu, Y., Nayakshin, S., & Rosotti, G. 2022, *MNRAS*, 515, 3113
 Esplin, T. L., & Luhman, K. L. 2019, *AJ*, 158, 54
 Facchini, S., Benisty, M., Bae, J., et al. 2020, *A&A*, 639, A121
 Facchini, S., Pinilla, P., van Dishoeck, E. F., & de Juan Ovelar, M. 2018, *A&A*, 612, A104
 Fang, M., Pascucci, I., Edwards, S., et al. 2023a, *ApJ*, 945, 112
 Fang, M., Wang, L., Herczeg, G. J., et al. 2023b, *NatAs*, 7, 905
 Fernandes, R. B., Mulders, G. D., Pascucci, I., Mordasini, C., & Emsenhuber, A. 2019, *ApJ*, 874, 81
 Fischer, W. J., Megeath, S. T., Furlan, E., et al. 2017, *ApJ*, 840, 69
 Flewelling, H. A., Magnier, E. A., Chambers, K. C., et al. 2020, *ApJS*, 251, 7
 Foreman-Mackey, D., Hogg, D. W., Lang, D., & Goodman, J. 2013, *PASP*, 125, 306
 Francis, L., Johnstone, D., Herczeg, G., Hunter, T. R., & Harsono, D. 2020, *AJ*, 160, 270
 Fulton, B. J., Rosenthal, L. J., Hirsch, L. A., et al. 2021, *ApJS*, 255, 14
 Gaia Collaboration, Vallenari, A., Brown, A. G. A., et al. 2023, *A&A*, 674, A1
 Gárate, M., Delage, T. N., Stadler, J., et al. 2021, *A&A*, 655, A18
 González-Ruilova, C., Cieza, L. A., Hales, A. S., et al. 2020, *ApJL*, 902, L33
 Guo, Z., Herczeg, G. J., Jose, J., et al. 2018, *ApJ*, 852, 56
 Hardegree-Ullman, K. K., Cushing, M. C., Muirhead, P. S., & Christiansen, J. L. 2019, *AJ*, 158, 75
 Hashimoto, J., Dong, R., & Muto, T. 2021, *AJ*, 161, 264
 Hendler, N., Pascucci, I., Pinilla, P., et al. 2020, *ApJ*, 895, 126
 Herczeg, G. J., & Hillenbrand, L. A. 2008, *ApJ*, 681, 594
 Herczeg, G. J., & Hillenbrand, L. A. 2014, *ApJ*, 786, 97
 Hildebrand, R. H. 1983, *QJRAS*, 24, 267
 Huang, J., Andrews, S. M., Dullemond, C. P., et al. 2018a, *ApJL*, 869, L42
 Huang, J., Andrews, S. M., Dullemond, C. P., et al. 2020, *ApJ*, 891, 48
 Huang, J., Andrews, S. M., Pérez, L. M., et al. 2018b, *ApJL*, 869, L43
 Jennings, J., Tazzari, M., Clarke, C. J., Booth, R. A., & Rosotti, G. P. 2022, *MNRAS*, 514, 6053
 Kraus, A. L., & Hillenbrand, L. A. 2012, *ApJ*, 757, 141
 Kraus, A. L., Ireland, M. J., Martinache, F., & Hillenbrand, L. A. 2011, *ApJ*, 731, 8
 Kurtovic, N. T., Pinilla, P., Long, F., et al. 2021, *A&A*, 645, A139
 Lantz, B., Aldering, G., Antilogus, P., et al. 2004, *Proc. SPIE*, 5249, 146
 Lauer, T. R., Ajhar, E. A., Byun, Y. I., et al. 1995, *AJ*, 110, 2622
 Martel, É., & Lesur, G. 2022, *A&A*, 667, A17
 Lesur, G. R. J. 2021, *A&A*, 650, A35
 Lin, J. W., Lee, E. J., & Chiang, E. 2018, *MNRAS*, 480, 4338
 Liu, B., Lambrechts, M., Johansen, A., & Liu, F. 2019, *A&A*, 632, A7
 Liu, Y. 2021, *RAA*, 21, 164
 Long, F., Andrews, S. M., Rosotti, G., et al. 2022, *ApJ*, 931, 6
 Long, F., Herczeg, G. J., Harsono, D., et al. 2019, *ApJ*, 882, 49
 Long, F., Pinilla, P., Herczeg, G. J., et al. 2018, *ApJ*, 869, 17
 Long, F., Ren, B. B., Wallack, N. L., et al. 2023, *ApJ*, 949, 27
 Longarini, C., Lodato, G., Bertin, G., & Armitage, P. J. 2023, *MNRAS*, 519, 2017
 Luhman, K. L. 2018, *AJ*, 156, 271

- Luhman, K. L., Allen, P. R., Espaillat, C., Hartmann, L., & Calvet, N. 2010, *ApJS*, **186**, 111
- Luhman, K. L., Mamajek, E. E., Shukla, S. J., & Loutrel, N. P. 2017, *AJ*, **153**, 46
- MacGregor, M. A., Weinberger, A. J., Wilner, D. J., Kowalski, A. F., & Cranmer, S. R. 2018, *ApJL*, **855**, L2
- Mairs, S., Lalchand, B., Bower, G. C., et al. 2019, *ApJ*, **871**, 72
- Manara, C. F., Ansdell, M., Rosotti, G. P., et al. 2023, in ASP Conf. Ser. 534, *Protostars and Planets VII*, ed. S. Inutsuka et al. (San Francisco, CA: ASP), 539
- Marton, G., Calzoletti, L., Perez Garcia, A. M., et al. 2017, arXiv:1705.05693
- Mercer, A., & Stamatellos, D. 2020, *A&A*, **633**, A116
- Miguel, Y., Cridland, A., Ormel, C. W., Fortney, J. J., & Ida, S. 2020, *MNRAS*, **491**, 1998
- Miotello, A., Kamp, I., Birnstiel, T., Cleevs, L. C., & Kataoka, A. 2023, in ASP Conf. Ser. 534, *Protostars and Planets VII*, ed. S. Inutsuka et al. (San Francisco, CA: ASP), 501
- Miranda, R., Muñoz, D. J., & Lai, D. 2017, *MNRAS*, **466**, 1170
- Morales, J. C., Mustill, A. J., Ribas, I., et al. 2019, *Sci*, **365**, 1441
- Mulders, G. D., Drażkowska, J., van der Marel, N., Ciesla, F. J., & Pascucci, I. 2021, *ApJL*, **920**, L1
- Mulders, G. D., Pascucci, I., & Apai, D. 2015, *ApJ*, **798**, 112
- Oke, J. B., & Gunn, J. E. 1982, *PASP*, **94**, 586
- Okuzumi, S., Momose, M., Sirono, S.-i., Kobayashi, H., & Tanaka, H. 2016, *ApJ*, **821**, 82
- Owen, J. E. 2020, *MNRAS*, **495**, 3160
- Owen, J. E., Clarke, C. J., & Ercolano, B. 2012, *MNRAS*, **422**, 1880
- Paneque-Carreño, T., Pérez, L. M., Benisty, M., et al. 2021, *ApJ*, **914**, 88
- Pascucci, I., Sterzik, M., Alexander, R. D., et al. 2011, *ApJ*, **736**, 13
- Pascucci, I., Testi, L., Herczeg, G. J., et al. 2016, *ApJ*, **831**, 125
- Pecaut, M. J., & Mamajek, E. E. 2013, *ApJS*, **208**, 9
- Pérez, L. M., Carpenter, J. M., Andrews, S. M., et al. 2016, *Sci*, **353**, 1519
- Pérez, S., Casassus, S., Hales, A., et al. 2020, *ApJL*, **889**, L24
- Picogna, G., Ercolano, B., & Espaillat, C. C. 2021, *MNRAS*, **508**, 3611
- Picogna, G., Ercolano, B., Owen, J. E., & Weber, M. L. 2019, *MNRAS*, **487**, 691
- Picogna, G., Schäfer, C., Ercolano, B., et al. 2023, *MNRAS*, **523**, 3318
- Pinilla, P. 2022, *EPJP*, **137**, 1206
- Pinilla, P., Birnstiel, T., Benisty, M., et al. 2013, *A&A*, **554**, A95
- Pinilla, P., Birnstiel, T., Ricci, L., et al. 2012, *A&A*, **538**, A114
- Pinilla, P., Kurtovic, N. T., Benisty, M., et al. 2021, *A&A*, **649**, A122
- Pinilla, P., Pascucci, I., & Marino, S. 2020, *A&A*, **635**, A105
- Pinilla, P., Pérez, L. M., Andrews, S., et al. 2017a, *ApJ*, **839**, 99
- Pinilla, P., Pohl, A., Stammer, S. M., & Birnstiel, T. 2017b, *ApJ*, **845**, 68
- Pinilla, P., Tazzari, M., Pascucci, I., et al. 2018, *ApJ*, **859**, 32
- Pinilla, P., van der Marel, N., Pérez, L. M., et al. 2015, *A&A*, **584**, A16
- Pollack, J. B., Hubickyj, O., Bodenheimer, P., et al. 1996, *Icar*, **124**, 62
- Rab, C., Weber, M. L., Picogna, G., Ercolano, B., & Owen, J. E. 2023, *ApJL*, **955**, L11
- Ragusa, E., Alexander, R., Calcino, J., Hirsh, K., & Price, D. J. 2020, *MNRAS*, **499**, 3362
- Ribas, I., Reiners, A., Zechmeister, M., et al. 2023, *A&A*, **670**, A139
- Rosotti, G. P., Booth, R. A., Tazzari, M., et al. 2019, *MNRAS*, **486**, L63
- Sanchis, E., Testi, L., Natta, A., et al. 2020, *A&A*, **633**, A114
- Schlecker, M., Burn, R., Sabotta, S., et al. 2022, *A&A*, **664**, A180
- Skrutskie, M. F., Cutri, R. M., Stiening, R., et al. 2006, *AJ*, **131**, 1163
- Somers, G., Cao, L., & Pinsonneault, M. H. 2020, *ApJ*, **891**, 29
- Stefánsson, G., Mahadevan, S., Miguel, Y., et al. 2023, *Sci*, **382**, 1031
- Suzuki, T. K., Ogihara, M., Morbidelli, A., Crida, A., & Guillot, T. 2016, *A&A*, **596**, A74
- Tazzari, M., Beaujean, F., & Testi, L. 2018, *MNRAS*, **476**, 4527
- Tazzari, M., Clarke, C. J., Testi, L., et al. 2021, *MNRAS*, **506**, 2804
- Tobin, J. J., Sheehan, P. D., Megeath, S. T., et al. 2020, *ApJ*, **890**, 130
- Trapman, L., Facchini, S., Hogerheijde, M. R., van Dishoeck, E. F., & Bruderer, S. 2019, *A&A*, **629**, A79
- Tripathi, A., Andrews, S. M., Birnstiel, T., & Wilner, D. J. 2017, *ApJ*, **845**, 44
- Tychoniec, Ł., Manara, C. F., Rosotti, G. P., et al. 2020, *A&A*, **640**, A19
- Valenti, J. A., Basri, G., & Johns, C. M. 1993, *AJ*, **106**, 2024
- van der Marel, N., & Mulders, G. D. 2021, *AJ*, **162**, 28
- van der Marel, N., van Dishoeck, E. F., Bruderer, S., et al. 2013, *Sci*, **340**, 1199
- van der Marel, N., Verhaar, B. W., van Terwisga, S., et al. 2016, *A&A*, **592**, A126
- van der Marel, N., Williams, J. P., Ansdell, M., et al. 2018, *ApJ*, **854**, 177
- van der Marel, N., Williams, J. P., Picogna, G., et al. 2022, arXiv:2204.08225
- van der Plas, G., Ménard, F., Ward-Duong, K., et al. 2016, *ApJ*, **819**, 102
- Villenave, M., Benisty, M., Dent, W. R. F., et al. 2019, *A&A*, **624**, A7
- Wafflard-Fernandez, G., & Lesur, G. 2023, *A&A*, **677**, A70
- Wang, L., Bai, X.-N., & Goodman, J. 2019, *ApJ*, **874**, 90
- Wang, S., & Chen, X. 2019, *ApJ*, **877**, 116
- Weber, P., Pérez, S., Zurlo, A., et al. 2023, *ApJL*, **952**, L17
- Wright, E. L., Eisenhardt, P. R. M., Mainzer, A. K., et al. 2010, *AJ*, **140**, 1868
- Yamaguchi, M., Tsukagoshi, T., Muto, T., et al. 2021, *ApJ*, **923**, 121
- Zhang, K., Blake, G. A., & Bergin, E. A. 2015, *ApJL*, **806**, L7
- Zhang, S., Kalscheur, M., Long, F., et al. 2023, *ApJ*, **952**, 108
- Zhu, W., & Dong, S. 2021, *ARA&A*, **59**, 291
- Zormpas, A., Birnstiel, T., Rosotti, G. P., & Andrews, S. M. 2022, *A&A*, **661**, A66